



저작자표시-비영리-변경금지 2.0 대한민국

이용자는 아래의 조건을 따르는 경우에 한하여 자유롭게

- 이 저작물을 복제, 배포, 전송, 전시, 공연 및 방송할 수 있습니다.

다음과 같은 조건을 따라야 합니다:



저작자표시. 귀하는 원저작자를 표시하여야 합니다.



비영리. 귀하는 이 저작물을 영리 목적으로 이용할 수 없습니다.



변경금지. 귀하는 이 저작물을 개작, 변형 또는 가공할 수 없습니다.

- 귀하는, 이 저작물의 재이용이나 배포의 경우, 이 저작물에 적용된 이용허락조건을 명확하게 나타내어야 합니다.
- 저작권자로부터 별도의 허가를 받으면 이러한 조건들은 적용되지 않습니다.

저작권법에 따른 이용자의 권리는 위의 내용에 의하여 영향을 받지 않습니다.

이것은 [이용허락규약\(Legal Code\)](#)을 이해하기 쉽게 요약한 것입니다.

[Disclaimer](#)

공학박사 학위논문

**Development of 3D printing process of shape
memory polymer composites**

형상기억고분자 복합재료의 3D 프린팅 공정 개발

2021 년 2 월

서울대학교 대학원

재료공학부

안 용 산

**Development of 3D printing process of shape
memory polymer composites**

Advisor: Woong-Ryeol Yu

by

Yongsan An

2021

Department of Materials Science and
Engineering Graduated School Seoul
National University

Development of 3D printing process of shape memory polymer composites

형상기억고분자 복합재료의 3D 프린팅 공정 개발

지도 교수 유 응 열

이 논문을 공학박사 학위논문으로 제출함

2020 년 12 월

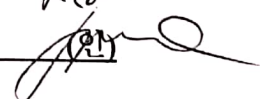
서울대학교 대학원

재료공학부

안 용 산

안용산의 공학박사 학위논문을 인준함

2020 년 12 월

위 원 장	안 철 희	
부 위 원 장	유 응 열	
위 원	이 명 규	
위 원	육 지 호	
위 원	나 원 진	

Abstract

Four-dimensional (4D) printing is a cutting edge technology in which the three-dimensionally printed objects change their shapes or properties over time. Shape memory polymer (SMP) is a representative material for 4D printing. New three-dimensional (3D) printing systems for SMPs are developed to improve and overcome the drawbacks of the existing 3D printing methods.

To characterize the 3D shape change of a 3D printed SMP, 3D characterization methods are suggested. The 3D deployment behavior of an SMP was quantitatively characterized using 3D shape descriptors. 3D shape descriptor is a numerical value which represents and analyzes the shape information of a given 3D shape. A 3D deployable antenna was designed and fabricated using an epoxy-based SMP. First, the folding behavior of the antenna was observed during deployment in a device. At this time, its entire shape was scanned, processed, and converted into surface data. Two-dimensional (2D) (area and circularity) and 3D (compactness and cubeness) shape descriptors were calculated from the surface data and compared to

determine if the 3D folding behavior of an SMP antenna could be adequately described by 3D compactness, which represents how compactly the SMP antenna was able to fold. In addition to 2D shape information, these data provide height information, resulting in a more accurate and sensitive characterization of the folding process. Finally, the 3D deployment behavior (folding-unfolding) of the SMP antenna was analyzed using a 3D descriptor. The shape fixation and recovery ratios of the SMP antenna according to the 3D descriptor were 100% and 99.5%, respectively, whereas those values evaluated with a one-dimensional descriptor, such as uniaxial strain, were 98.0% and 79.1%, respectively. These results demonstrate that a 3D descriptor (compactness) can adequately assess shape memory performance.

An SMP has poor mechanical property so that an SMP composite (SMPC) has been studied and used in various applications. Continuous carbon fiber is the most effective reinforcing material to give great mechanical properties. In order to print the continuous carbon fiber-reinforced thermoplastic (CCFRTP) SMP three-dimensionally, a new 3D printing system was developed. CCFRTPs, which are popular due to their light weight and high strength, are typically fabricated using heavy and expensive equipment. Recently, 3D printing has been used for efficient production of small CCFRTPs. In this study, the 3D printing system was developed based on *in situ* pin-assisted melt

impregnation in the printing head, i.e., melt impregnation and printing processes in one pot. Printing conditions were investigated by evaluating the printability and degree of impregnation. The tensile strength of specimens printed using the new printing system was compared with that of specimens printed using other printing methods. The uniformly impregnated CCFRTP printed case specimens had superior mechanical properties. Finally, an SMPC antenna was 3D printed and its 3D shape memory properties were characterized by 3D deployment test.

Among 4D printing materials, thermosetting polymers are useful for various applications due to their high mechanical properties, thermodynamic stability, excellent chemical resistance, and solvent resistance. Using a thermosetting material capable of frontal polymerization, a free-standing structure could be 3D printed which can enlarge the complexity of the shape. In this study, an SMP capable of frontal polymerization was synthesized by adding cyclooctene as a monomer to form switching segments in a poly(dicyclopentadiene) network. As a result of thermomechanical analysis of the material, it was confirmed that it shows shape memory behavior. The rheological properties of the material was controlled to have an effective homogeneous shear modulus for printing a free-standing structure. A hexagonal spiral with free-standing structure was successfully printed using the 3D printing system.

The printed product showed good shape memory performance.

Keywords: Shape memory polymer composites, shape descriptor, continuous fiber-reinforced polymer composites, 4D printing, frontal polymerization

Student number: 2015-20839

Contents

Abstract.....	i
Contents.....	v
List of Tables.....	viii
List of Figures.....	ix
1. Introduction.....	1
1.1. Shape memory polymers.....	1
1.2. 4D printing: 3D printing of shape memory polymers.....	3
1.3. 3D printing methods of shape memory polymers.....	4
1.4. Research objectives.....	7
2. 3D characterization of 3D deployable shape memory polymer composites.....	9
2.1. Preparation of 3D deployable SMPC.....	12
2.1.1. Preparation and 1D shape memory test of SMP.....	12
2.1.2. Multi-dimensional deployment test of SMP.....	18
2.2. 3D characterization via 3D shape descriptors	21
2.3. Multi-dimensional shape memory properties of SMP.....	24
2.3.1. Thermomechanical properties of SMP	24
2.3.2. Multi-dimensional shape memory properties.....	30
2.3.3. Shape memory properties of deployable SMP.....	37
2.5. Summary.....	41

3. 3D printing process of thermoplastic shape memory polymer composites.....	42
3.1. Preparation of a new 3D printing system.....	43
3.1.1. Design of the new printing system.....	43
3.1.2. Materials and printed samples.....	47
3.1.3. Characterization.....	48
3.2. 3D printing of CCFRTPs.....	49
3.2.1. Printability of the new printing system.....	49
3.2.2. Degree of impregnation of the CCFRTPs.....	55
3.2.3. Mechanical properties of the CCFRTPs.....	59
3.3. 3D printing and 3D characterization of SMPCs.....	64
3.4. Summary.....	68
4. 3D printing process of thermosetting shape memory polymers.....	69
4.1. Preparation of a new 3D printing system.....	71
4.1.1. Materials and sample preparation.....	71
4.1.2. Characterization.....	72
4.1.3. 3D printing process.....	74
4.2. 3D printing of the thermosetting SMP.....	74
4.2.1. Thermomechanical and shape memory properties.....	74
4.2.2. Rheological properties and frontal velocity.....	79
4.2.3. 3D printing and the shape memory properties of SMP.....	86
4.3. Summary	90
5. Conclusions.....	91

Reference.....	93
Korean abstract.....	104

List of Tables

Table 2-1 Characterization methods of SMPs in various applications.

Table 2-2 Multi-dimensional shape memory properties of SMP.

Table 2-3 Tensile properties of SMPC

Table 2-4 Thermal properties of the SMP and SMPC

Table 2-5 2D and 3D shape descriptors of virtual antennas in figures 7(a)–(f).

Table 2-6 2D and 3D shape descriptors of virtual antennas in figures 8(a)–(d).

Table 2-7 3D shape memory properties of the SMP antenna.

Table 3-1 Printability of CCFRTPs by the 3D printer using *in situ* pin-assisted melt impregnation under various printing conditions. Printability was classified as follows: the composite was printable (printable), the nozzle was clogged (clogged), the fiber was damaged or broken (damaged), or the composite strand was not attached to the build plate (not attached).

Table 3-2 Tensile properties of CCFRTPs made with various matrix materials 3D-printed by the *in situ* pin-assisted melt impregnation 3D printer.

Table 3-3 Shape memory properties of SMPC antenna.

Table 4-1 Thermomechanical and shape memory properties of SMP.

List of Figures

Figure 2-1 Scheme of the fabrication process of SMP specimens

Figure 2-2 Scheme of the fabrication process of SMPC specimens

Figure 2-3 1D shape memory test of SMP. (a) Universal testing machine with a heat chamber for cyclic thermomechanical tensile tests, (b) typical stress–strain curve, (c) 3D plot of stress–strain-temperature.

Figure 2-4 3D shape memory test of shape memory polymers via a 3D deployment test. (a) Folding device, (b) folding process, and (c) schematics of the deployment test.

Figure 2-5 Scanning of 3D shape of shape memory polymers and calculation of the shape descriptors.

Figure 2-6 Thermodynamic curve of SMPC obtained using DMA.

Figure 2-7 Stress-strain curve of SMPC (a) below the transition temperature and (b) above the transition temperature

Figure 2-8 Cyclic thermomechanical behavior of SMP obtained using UTM.

Figure 2-9 Absorptivity of SMPC and solar irradiance in low earth orbit

Figure 2-10 (a)–(f) 3D model and their 2D projected surface in the vertical direction, (g) 2D shape descriptors of the given shapes, and (h) 3D shape descriptors of the given shapes.

Figure 2-11 3D model and their 2D projected surface for comparison of 2D and 3D shape descriptors. (a) 2-fold model, (b) 2-fold-2-layer model, (c) 4-fold model, (d) 8-fold model, (e) 2D and 3D shape descriptors of the given shapes.

Figure 2-12 3D model of the SMP antenna during the deployment test, which was

obtained by scanning its shape, and their 2D projected surface. (a) Original shape, (b) deformed shape, (c) temporary shape, (d) recovered shape.

Figure 3-1 Previously developed 3D-printing system for CCFRTPs. (a) Commercial 3D printer (Mark Two [70]) and (b) in-nozzle impregnation 3D printer ([71]).

Figure 3-2 3D-printing system for CCFRTPs developed in this study. (a) Schematic illustration showing the *in situ* pin-assisted melt impregnation printing head, (b) actual printing system, and (c) inside of the heating block showing the pins.

Figure 3-3 (a) Differential scanning calorimetry curves of the matrix filaments and (b) viscoelastic properties of the nylon filament.

Figure 3-4 (a) Well-printed composite strand, (b) damaged composite strand, and (c) cross-sections of composite strands.

Figure 3-5 Cross-sections of nylon-impregnated composite filaments. (a) Impregnated and non-impregnated regions using (b) 0, (c) 2, and (d) 4 pins.

Figure 3-6 Relationship between the (a) temperature and degree of impregnation (DOI) (printing speed = 100 mm/min; number of pins = 2), (b) printing speed and DOI (printing temperature = 260°C; number of pins = 2), and (c) number of pins and DOI (printing temperature = 260°C; printing speed = 100 mm/min).

Figure 3-7 Tensile test results of the nylon-impregnated composite strands.

Figure 3-8 (a) Tensile test results of the 3D-printed tensile specimens. Failure of 3D-printed tensile specimens printed by the (b) Mark Two printer, (c) in-nozzle impregnation 3D printer, and (d) *in situ* pin-assisted melt impregnation 3D printer equipped with four pins.

Figure 3-9 (a) 3D printing of SMPC antenna, (b) 3D printed SMPC antenna, and (c) 3D scanning of the deployment process using 3D scanner.

Figure 3-10 The 3D scanned image during the deployment test. (a) Original shape, (b) deformed shape, (c) temporary shape, and (d) recovered shape.

Figure 4-1 (a) Schematic diagram of frontal polymerization and (b) polymerization mechanism and chemical structure of frontal SMP.

Figure 4-2 TGA analysis of SMP according to CO content.

Figure 4-3 (a) Thermomechanical behavior of SMP according to CO content (straight line - storage modulus, dash line - tan delta) and (b) shape memory behavior (CO content: 0.15 mol equivalent to DCPD).

Figure 4-4 (a) Rheological properties of SMP and (b-g) extruded appearance at each state.

Figure 4-5 (a) Frontal polymerization of frontal SMP ink, (b) IR camera image for frontal velocity measurement (c) frontal velocity according to incubation time.

Figure 4-6 (a) Schematic diagram of printing head, (b) 3D design of free-standing structure and (c) printed product using 3D printing.

Figure 4-7 Shape memory behavior of 3D printed frontal SMP under (a) tensile deformation and (b) compressive deformation.

Chapter 1. Introduction

1.1. Shape memory polymers

Shape memory polymers (SMPs) are smart materials that can return to their original shape after a temporary deformation in response to an external stimulus, such as temperature. SMPs are attracting attention as alternatives to shape memory alloys because they have light weight, large deformability, inexpensive cost, great recovery and potential in biocompatibility [1]. In this respect, SMPs are used in the field of robotic actuator [2-5], in the aerospace applications for deployable solar arrays or reflector antennas [6-12], in the area of self-transformable electronic devices [13-17], and in the biomedical applications such as sutures and stents [18-22]. Recently, several researchers studied three-dimensional (3D) deployment structures, such as a deployable antenna [23-25] and actuators manufactured by so-called four-dimensional (4D) printing [26-30].

SMPs shows shape memory behavior by various external stimulus. The possible actuation stimuli are heat, stress, electrical voltage, magnetic field, light, chemical changes such as pH etc [31]. SMPs are categorized as thermo-, mechano-, electro-, magneto-, photo-, and chemo-, and photo-responsive SMPs according to the corresponding stimuli [32]. Most of SMPs are thermo-responsive, or thermo-responsive shape memory effect becomes the basic mechanism of other stimuli-responsive SMPs [12]. The types of stimulus are important in application. Especially

in aerospace, thermo- and electro-responsive SMPs were widely used. Deployable hinges [33-36], truss booms [37-39], solar arrays [40, 41], deployable reflector antennas [23-25], morphing wings [42, 43], and expandable lunar habitat [44, 45] were investigated using SMPs due to their low cost, lightweight, and self-transformability. Triggers of SMP can be the solar radiation, electrical current, or other heat suppliers. Because SMPs triggered by the solar radiation have an advantage that they do not need other power devices, the main challenge was to develop SMPs which have high strength and actuate properly within the temperature range achieved by solar radiation.

As SMPs become more widely applied, it is essential to quantitatively measure 3D shape changes to evaluate deployment performance. Many researchers have evaluated the shape memory performance of thermo-responsive SMPs using 'cyclic thermomechanical tensile test [46]'. This method applies uniaxial tensile strain to an SMP above its transition temperature and then fixes the shape by lowering the temperature. An external stimulus such as heat is then applied to restore the tensile strain. The mechanism of the shape memory behavior during the test can be explained thermodynamically [31, 47]. Above the transition temperature, the polymer chain segments are flexible so that the SMP can be stretched with a decrease in entropy [48]. When cooling below the transition temperature, strain-induced crystallization of the polymer chain fixes its temporary shape. Here, shape fixation performance was measured. Then the SMP is heated above the transition temperature and recover its permanent shape in order to restore its high entropy state [31]. In this

process, shape recovery performance was measured.

In practical uses, an SMP plays a role by changing its shape so that it is necessary to utilize origami or to design and manufacture geometrically complex shape according to the purpose. For this, 3D printing was suggested as a manufacturing tool of SMP.

1.2. 4D printing: 3D printing of shape memory polymers

When an SMP is 3D printed, it is called 4D printing. 4D printing refers to the addition of one-dimension (i.e. time) to 3D printing [49]. The 3D printed objects change their shape, properties, or perform various functions over time [49]. The materials mainly used for 4D printing are hydrogels [27, 50-53] and SMPs [54-58]. In case of hydrogel, a swellable hydrogel and a non-swellable polymer are printed. When the printed product is put in a solvent, its shape changes because the two materials show different degree of swelling [55]. Hydrogel based 4D printing has the disadvantages that the mechanical properties and the actuating force generated by shape changing are weak, the response speed is slow, and the usage environment is limited to the solvent [55]. On the other hand, SMPs have high strength and actuating force, fast response speed so that SMPs have the wide range of application. However, it requires a programming process after printing. As mentioned above, the utility of SMP can increase when a proper actuating force is generated through the deformation of geometrically complex shapes. 3D printing makes it possible. With a proper design, a complex shape can be 3D printed and a programming process can be performed

with a simple action [55].

1.3. 3D printing methods of shape memory polymers

SMPs have poor mechanical properties so that SMP composites (SMPCs) are used in various applications. Especially, carbon fiber-reinforced SMPCs are fabricated to enhance their strength. Carbon fiber-reinforced polymer composites are of great interest as substitutes for steel and aluminum because of their light weight, high specific stiffness, and strength. They are widely used whenever improved energy efficiency is sought through weight reduction. Applications include aerospace, automobile, construction, and sporting goods [59-62]. Carbon fiber-reinforced thermoplastic (CFRTP) composites have low processing cost and are easier to recycle than thermosetting composite materials. In addition, they have excellent impact resistance, corrosion resistance, and chemical resistance [59, 62-64]. Carbon fibers, which are used for reinforcing composite materials, are classified as short, long, or continuous fibers according to their length. Continuous CFRTPs (CCFRTPs) have the advantages of being the strongest and stiffest fibers in the longitudinal direction, but their manufacture is difficult and complex shapes can be challenging to form. CCFRTPs are fabricated using conventional manufacturing methods, including injection molding, compression molding, rotational molding, vacuum forming, extrusion, pultrusion, and bladder-assisted molding [62, 65]. However, these manufacturing processes require heavy and costly equipment, and molds for

complex-shaped products can be very expensive. Furthermore, it is not routine to create complex shapes having the desired fiber orientation using conventional manufacturing processes.

To overcome these manufacturing limitations, three-dimensional (3D) printing has been suggested for fabricating CCFRTPs [63, 65-71]. A commercial 3D printer has been developed that can print these composites using prepreg filaments composed of nylon matrix with continuous carbon fiber for reinforcement [68, 70]. Continuous-fiber 3D printers have also been developed, based on an automated tape-laying process [72, 73]. These devices used impregnated tapes or filaments, which are laid down on the build plate. Furthermore, in-nozzle impregnation has been applied to a 3D-printing system in which continuous fibers were impregnated by thermoplastic filaments within the nozzle of the print head [67, 71, 74-76]. Continuous-fiber printed parts have higher strength and modulus than pure polymer parts or short fiber-reinforced polymer composite parts manufactured by 3D printers [67, 71].

It is uneconomical to use impregnated tapes or fibers for printing CCFRTPs, because the prepreg filaments or tapes need to be manufactured before printing. Furthermore, the ability to use fibers and matrix materials may be limited if prepreg filaments or tapes are not available in the form required. In this respect, a 3D-printing system equipped for in-nozzle impregnation would seem to be beneficial. However, poor impregnation and interfacial properties can lead to poor mechanical properties if the impregnation path is too short for the fibers to be heated and sufficiently impregnated

[71, 77]. To overcome this issue, a screw extruder was used for in-nozzle impregnation [78], but this required large, heavy, and costly equipment. Therefore, it is need to develop new 3D printing system for CCFRTPs, which is applicable to printing thermoplastic SMP composites.

Among 3D printing materials, thermosetting polymers are useful for various applications due to their thermodynamic stability, excellent chemical resistance, and solvent resistance [79, 80]. However, unlike thermoplastic polymers that can be 3D printed simply by fused deposition modeling (FDM), thermosetting polymers have limited printing methods. In stereolithography apparatus (SLA) and digital lighting processing (DLP), a product is printed by irradiating light on a liquid photocurable resin layer by layer. In material jetting, a photocurable resin is sprayed onto the substrate after which a light is irradiated on it to cure the resin [81]. In both cases, the materials are limited to photocurable resins. Recently, a method of modifying the rheological properties of thermosetting resin to be suitable for 3D printing, and undergoing a post-curing after 3D printing has been developed [82]. However, this method has the disadvantage that the post-curing process takes a long time from 4 to 24 hours [80, 82-84]. Therefore, it is also need to develop a new 3D printing system for thermosetting SMPs.

1.4. Research objectives

4D printing is a cutting-edge technology that prints SMP and it changes its shape as time goes by. In order to increase the functionality of 4D printing, SMP must be able to withstand a high external load, and printed into geometrically complex shapes. Therefore, it is need to develop a new 3D printing method for SMP and SMPCs.

In Chapter 2, a method for characterizing 3D deployable SMPs were suggested. In 4D printing, SMPs are printed in complex 3D shapes, but conventional characterization methods cannot accurately measure and evaluate the 3D shape changes. Here, the 3D shape change of an SMP was quantitatively measured for proper usage using a computational tool called a shape descriptor. For this, SMP was fabricated, the deployment test was performed, 3D shape changes were observed with a 3D scanner, and the 3D shape memory properties were analyzed.

In Chapter 3, a new 3D printing process for CCFRTPs was developed. The process was designed by introducing pin-assisted melt impregnation. The printability of the process was analyzed and the degree of impregnation and the mechanical properties of printed products were measured. Finally, the continuous carbon fiber-reinforced SMPC was 3D printed and its 3D shape memory properties were characterized.

In Chapter 4, a new 3D printing process was developed to print free-standing thermosetting SMP. For this, an SMP capable of frontal polymerization was synthesized and it was confirmed that the new material shows shape memory behavior. The 3D printing conditions were determined by analyzing the rheological

properties and frontal polymerization velocity of SMP. Finally, the SMP with free-standing structure was printed and the shape memory property was characterized.

Chapter 2. 3D characterization of 3D deployable shape memory polymer composites

Shape memory property is usually characterized by 'cyclic thermomechanical tensile test.' Such one-dimensional (1D) characterization methods employ uniaxial tensile deformation and assess shape memory performance by measuring changes in the length of the object. Two-dimensional (2D) characterization methods have been based on flexural strain [35, 85, 86], the bending angle [26, 29, 35, 87, 88] and curvature [27, 28, 30], and the x and y coordinates of a particular point [29]. However, 1D and 2D characterization methods can only display local changes or provide piecemeal information on 3D shape changes. Neither 1D nor 2D methods can correctly account for 3D shape changes. 3D characterization methods have been based on 3D volume changes [89], 3D coordinate changes of several points [23], wrinkle restoration, wrinkle preservation, and plan shape [90, 91]. While these methods have been employed in a variety of applications (Table 2-1), they are not sufficient to quantitatively characterize 3D shape changes as required for aerospace, biomedical and 4D printing applications. Therefore, a new 3D characterization technique is needed to adequately and quantitatively describe shape information and shape memory properties.

Table 2-1 Characterization methods of SMPs in various applications.

Dimension of Shape change	Application	Factor for characterization	Reference
1D	Truss structure	1D displacement	[92]
2D	Deployable hinge	2D angle	[35, 93]
	Tape spring	2D angle	[89]
	Morphing wing	2D angle	[43]
		1D displacement	[42]
3D	Reflector of antenna	Change of the 3D coordinates of multiple points	[23]
	Cardiovascular stent	1D displacement	[94]
	Fabric	3D wrinkle recovery 3D crease retention 3D flat appearance	[90, 91]
	Foam	3D volume change	[89]
		1D radius change	[95]
		1D shrinkage	[96, 97]
	Self-folding flower, finger	2D curvature	[30]
	4D printed flower	2D curvature	[27, 28]
Deployable 3D box	2D hinge angle	[26]	

In this chapter, 3D deployment behavior was characterized using a new 3D characterization method based on a shape descriptor. A shape descriptor is a computational tool for analyzing the shape information of a given object, and is expressed numerically using a mathematical formula to describe a specific characteristic of a given shape [98]. For example, convexity, a 2D shape descriptor, is calculated as the ratio of the area of a given shape to the area of a convex hull and indicates how convex the shape is [99]. Many 2D descriptors have been studied,

including area, roundness, convexity, rectangularity, and ellipticity. Several 3D descriptors have also been examined, including image moment, compactness, and cubeness [92, 94, 99-101]. This study evaluates a shape descriptor that describes the functional aspects of 3D deployable objects.

Among many possible applications, we have chosen to examine a deployable reflector antenna used in aerospace applications and searched for a 3D shape descriptor suitable for a full evaluation of SMP behavior. A parabolic antenna is usually used for satellite communication due to their high directivity [95]. In aerospace application, the parabolic antennas have been designed to be deployable because the structures have the advantage of transportability. The deployable antennas are folded before they are loaded in a vehicle to improve its transportability. After the vehicle arrived at space, the antennas are deployed by an external force. Using SMPs, the reflectors can be deployed with their own recovery force which is thermally induced by solar radiation. The use of SMP antennas can enhance fuel efficiency because they are lightweight and exhibit large deformation and excellent self-transformability [23, 24, 93]. In order to compensate for the shortcomings of SMPs with low mechanical properties and low thermal conductivity, SMPCs were manufactured by searching for reinforcing materials. In particular, the method of manufacturing SMPCs using nano-reinforcement was studied, and the mechanical and thermal properties were measured and evaluated. In this study, an SMPC antenna was fabricated and its 3D deployment, which consisted of a folding-unfolding process, was examined. For this, the 1D shape memory property was expanded to

multi-dimensional shape memory properties by using shape descriptors. Several known shape descriptors were investigated and the 3D deployment behaviors of the antennas were quantitatively evaluated.

2.1. Preparation of 3D deployable SMP

2.1.1. Preparation and 1D shape memory test of SMP

SMP was fabricated from an epoxy resin (YD-128; Kukdo Chemical Co., Ltd, Korea) and a hardener, 4,4'-diaminodiphenylmethane (DDM; Sigma-Aldrich, Inc., USA), used as received at a weight ratio of 100:18. The mixture was stirred using a magnetic bar for 10 min at 600 rpm in an oil bath at 90°C. After the solid hardener had completely dissolved in the epoxy resin, the mixture was degassed in a vacuum oven for 10 min at 40°C. After degassing, the mixture was poured into a mold and cured at 150°C for 120 min, and then for an additional 60 min at 180°C (Figure 2-1).

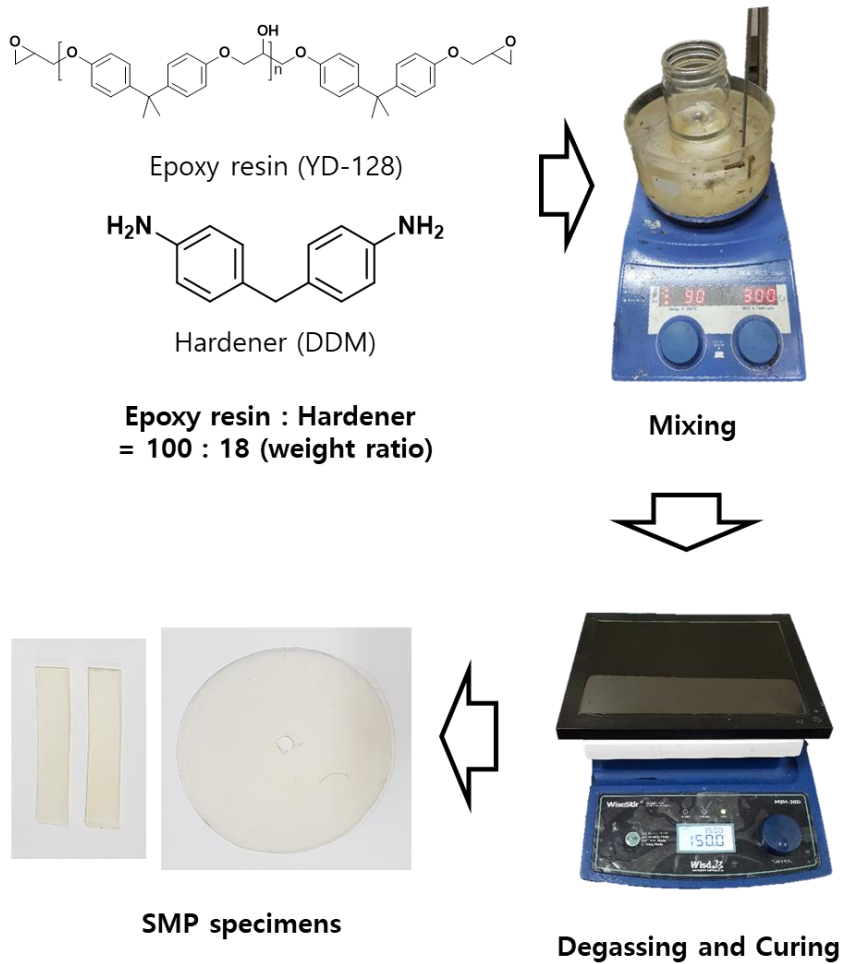


Figure 2-1 Scheme of the fabrication process of SMP specimens

SMPC was prepared following the method shown in 오류! 참조 원본을 찾을 수 없습니다.. Firstly, epoxy resin and multi-walled carbon nanotube (MWCNT, MR99, Carbon Nano-material Tech. Co., LTD, Korea, carbon purity ~99%) were weighed, mixed, and mechanically stirred at 90 °C for 30 minutes with a tip sonicator (VCX-

750, 750 Watts Ultrasonic processor, YOUNG-JIN Co., LTD.). The tip sonication was performed for 60 minutes under the condition of pulse 5/15 seconds and amplitude 30%. After degassing at room temperature for 60 minutes, the hardener was added at 90°C and mechanically stirred for 10 minutes. After the hardener was completely mixed, the mixture was degassed in vacuum condition at 40°C for 10 minutes. The mixture was casted on a 1 mm-thick mold and cured at 150 °C for 120 minutes and 180°C for 60 minutes. The weight ratio of MWCNTs were 0.5 wt%.

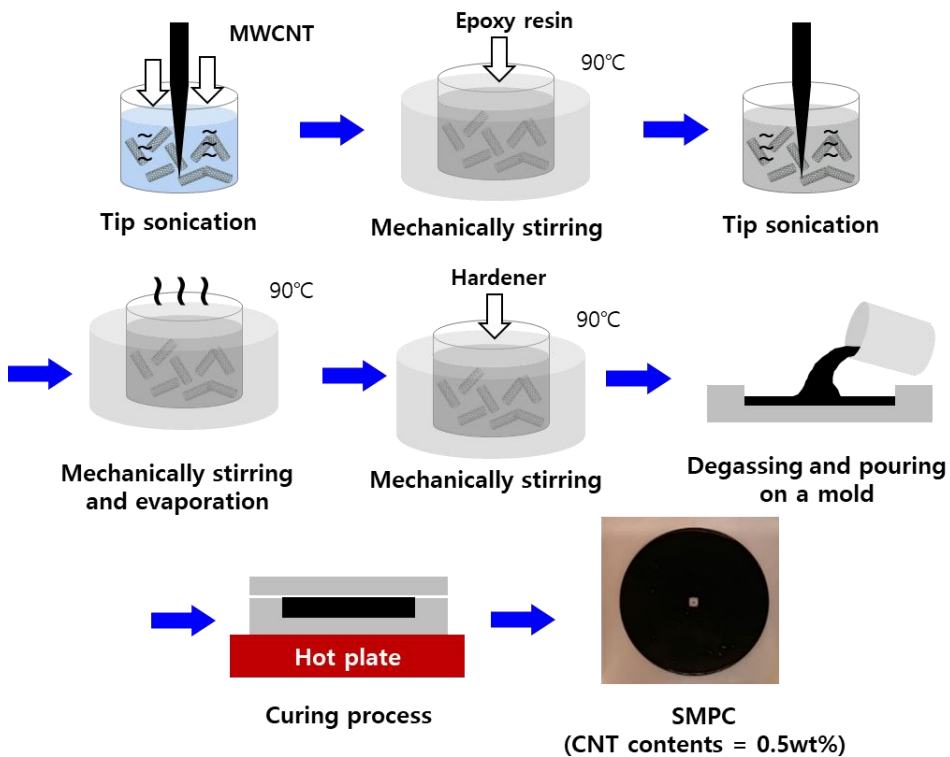


Figure 2-2 Scheme of the fabrication process of SMPC specimens

The activation conditions of the SMP were determined by measuring its transition temperature (T_s), storage modulus, and tangent delta using a dynamic mechanical analyzer (DMA) (Q800; TA Instruments, Inc.) and tensile mode-oscillation tests. The gage length of SMP specimens was 10 mm. A dynamic load (maximum load = 0.001 N, frequency = 1 Hz) was applied to each specimen, during which the temperature was ramped from 25°C to 160°C at 5°C min⁻¹.

Thermal properties of SMP was characterized. The specific heat was calculated from the DSC data (200 F3 Maia, NETZSCH, Germany) and the thermal conductivity was measured by Laser Flash Apparatus (LFA 457, NETZSCH, Germany). The absorptivity in the range of 200~2700nm was measured via UV-Vis spectroscopy (V-770, JASCO Corp., Japan).

To characterize the mechanical properties of SMPC, tensile tests were performed in an environment below the transition temperature and above the transition temperature using a universal testing machine (QUASAR 5; Galdabini) according to ASTM D-638 standard.

The shape memory performance of the SMP was characterized by the cyclic thermomechanical tensile test. For this, SMP specimens were cut to 1 × 10 × 50 mm with a gage length of 30 mm and the test was conducted 3 times. All tests were performed with a universal testing machine in an environmental chamber (오류! 참조 원본을 찾을 수 없습니다.(a)). A typical stress–strain curve and a 3D plot with stress, strain, and temperature are shown in 오류! 참조 원본을 찾을 수 없습니

Fig. (b) and (c). First, the specimens were elongated by 10% at 3 mm min⁻¹ above their transition temperature (130°C) (①). The specimens were cooled below their transition temperature (30°C) at 5°C min⁻¹, in order to fix their temporary shapes (②). Then the specimens were unloaded (③). Together, this process is called 'shape memory programming'. Then, the specimens were brought back to their original shape by heating to 130°C at 5°C min⁻¹ (④). This final step is called 'recovery'. During these programmed tensile tests, shape fixity and recovery ratios were calculated using the following equations

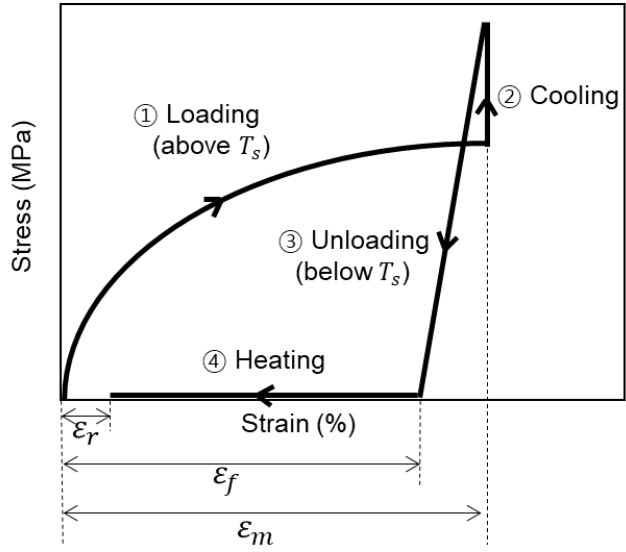
$$\text{Shape fixity ratio, } R_f = \frac{\varepsilon_f}{\varepsilon_m} \quad (1)$$

$$\text{Shape recovery ratio, } R_r = \frac{\varepsilon_m - \varepsilon_r}{\varepsilon_m} \quad (2)$$

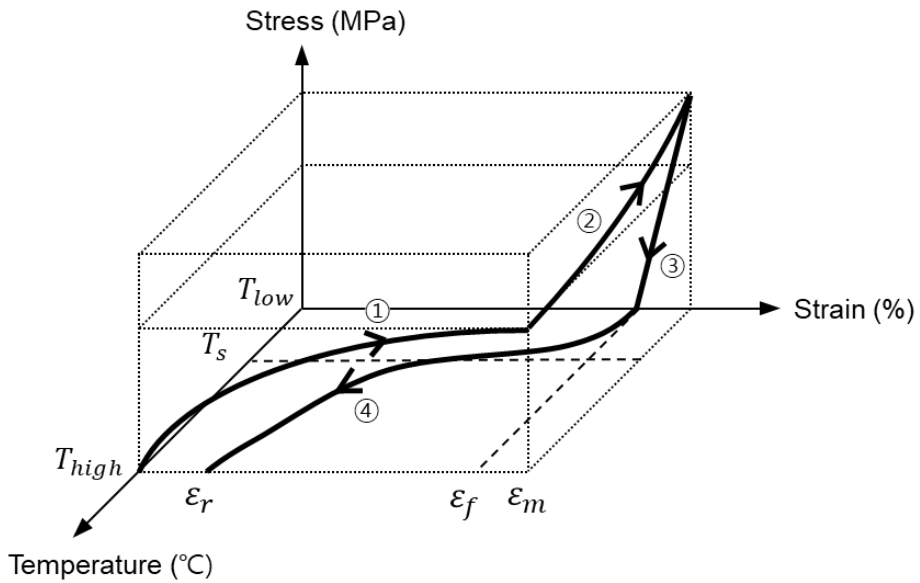
where ε_m is the applied strain, ε_f is the strain after the fixation (by cooling and unloading), and ε_r is the strain after the recovery. The 'shape fixity ratio' shows the degree to which the SMP shape is fixed after deformation and the 'shape recovery ratio' shows the degree to which the SMP returns to its original shape. These two values are used as measures of inherent performance, i.e., shape memory performance based on uniaxial deformation.



(a)



(b)



(c)

Figure 2-3 1D shape memory test of SMP. (a) Universal testing machine with a heat chamber for cyclic thermomechanical tensile tests, (b) typical stress–strain curve, (c) 3D plot of stress–strain–temperature.

2.1.2. Multi-dimensional deployment test of SMP

Deployable antennas must fold compactly for transportability and then be restored to their original shape for good performance when needed. Therefore, 3D deployment tests were performed with a miniature model of a parabolic reflector antenna, made from our SMP, to characterize its folding-unfolding behavior. A flat circular antenna was manufactured instead of paraboloid for convenience. The diameter and thickness of the antenna were 150 mm and 1.1 mm, respectively. Three specimens were prepared for the deployment tests. The antenna was installed in a folding device designed and fabricated for these deployment experiments (Figure 2-4(a) and (b)). The deployment process is shown in Figure 2-4(c). The antenna of original shape was heated to a high temperature (130°C) and the antenna was folded using the folding device at high temperature. Then the antenna was cooled to a low temperature (30°C) while maintained on the device in the folded configuration. After that, the antenna was removed from the device. The antenna maintained its shape without the aid of the folding device. Finally, the antenna was restored to its original shape as the temperature rose to 130°C. The shape of the antenna during the course of these four steps (before deformation, high temperature folding, fixing after cooling, and heating/recovery) was measured using an optical 3D scanner (ATOS Core 500; GOM). The measured data were used to obtain characteristic parameters after image processing (Figure 2-5). Projected surface information in the vertical direction was used for 2D characterization and the voxel representation of the geometry was used for 3D characterization. Figure 2-5 shows how the shape

descriptor was calculated from the measured data.

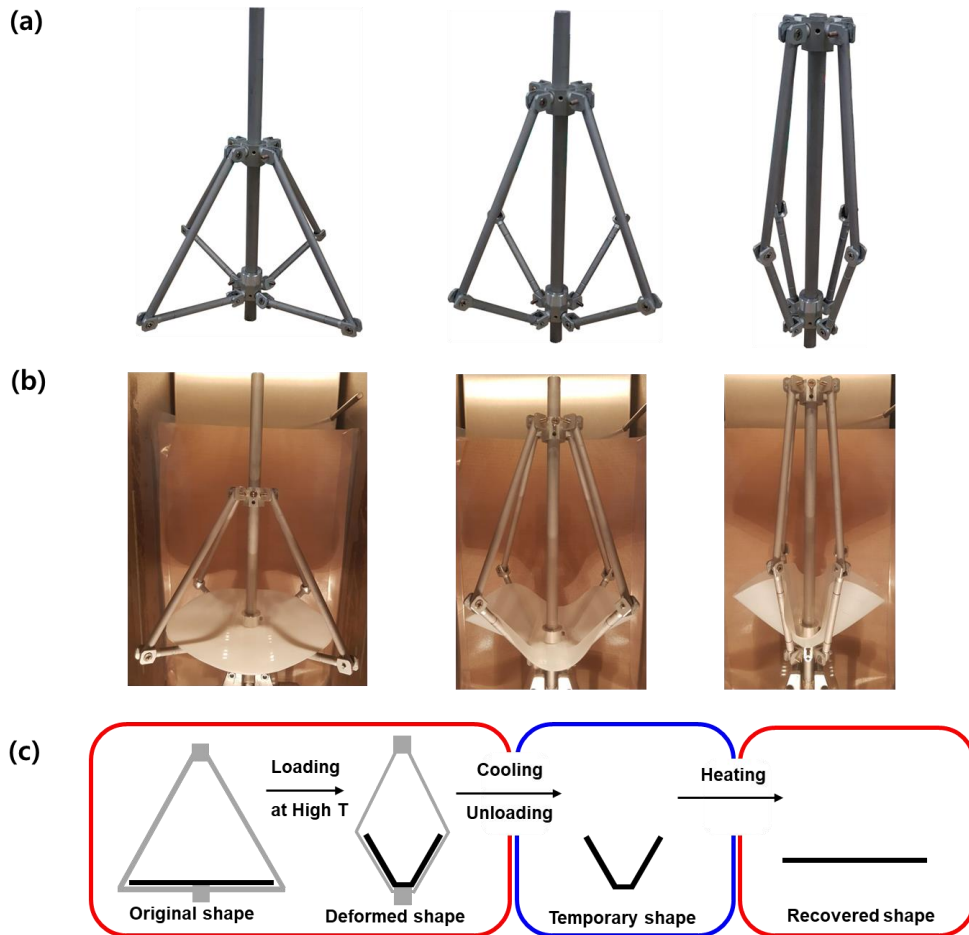


Figure 2-4 3D shape memory test of shape memory polymers via a 3D deployment test. (a) Folding device, (b) folding process, and (c) schematics of the deployment test.

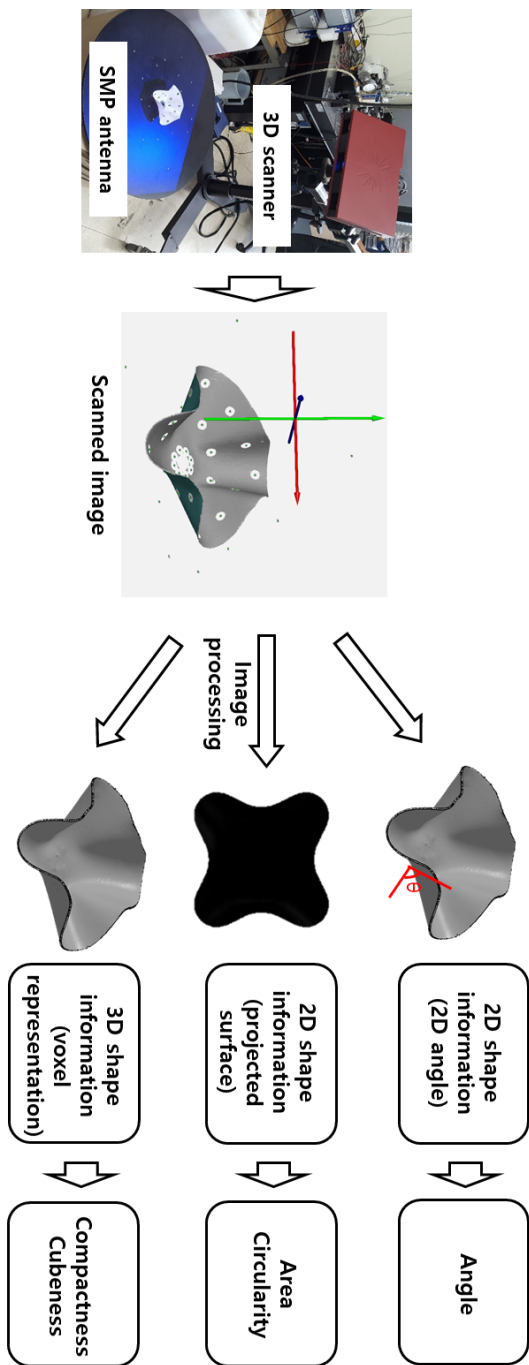


Figure 2-5 Scanning of 3D shape of shape memory polymers and calculation of the shape descriptors.

2.2. 3D characterization via 3D shape descriptors

For comparison, we first performed a 2D characterization using angle variation, which shows the degree to which the antenna was folded, to evaluate the deployment behavior of the antenna (Figure 2-5). We also obtained 2D geometry descriptors, such as area and circularity, by measuring the projected surface of the deployed antenna in the vertical direction. Projected area is a measure of how much space is on a flat surface. For example, a smaller surface area represents a compactly folded antenna. Circularity is a measure of the degree of similarity between a given shape and a perfect circle, calculated according to the following equation:

$$\text{Circularity, } C = 4\pi \times \frac{(\text{Area})}{(\text{Perimeter})^2} \quad (3)$$

These shape descriptors were calculated from the scanned data of the four states mentioned in section 2.1.2.

Compactness and cubeness were used for 3D characterization. As compactness is based on Euclidean distance, with the most compact shape being a sphere, this descriptor shows the extent to which a given shape is similar to a perfect sphere using a numeric value from 0 to 1 [98]. Similarly, cubeness is based on chessboard distance, where the most compact shape is a cube, and is given as a numeric value from 0 to 1. Standard compactness can be calculated using the following equation

$$\text{Standard compactness, } C^S = \frac{36\pi \times (\text{Volume})^2}{(\text{Surface})^3} \quad (4)$$

Zunic [100] suggested a compactness based on the moment and stated that the compactness, C^Z is suitable for describing a folding shape as follows,

$$\text{Compactness based on the moment, } C^Z = \frac{3^{5/3}}{5(4\pi)^{2/3}} \times \frac{(\mu_{0,0,0})^{5/3}}{\mu_{2,0,0} + \mu_{0,2,0} + \mu_{0,0,2}} \quad (5)$$

where

$$\text{Moment, } m_{p,q,r} = \iiint_S x^p y^q z^r dx dy dz$$

$$\text{Central moment, } \mu_{p,q,r} = \iiint_S (x - \bar{x})^p (y - \bar{y})^q (z - \bar{z})^r dx dy dz$$

$$\text{where } (\bar{x}, \bar{y}, \bar{z}) = \left(\frac{m_{1,0,0}}{m_{0,0,0}}, \frac{m_{0,1,0}}{m_{0,0,0}}, \frac{m_{0,0,1}}{m_{0,0,0}} \right) .$$

Martinez-Ortiz [101] proposed cubeness, calculated by the following equation,

$$\text{Cubeness, } C^M = \frac{3}{8} \times \frac{(\text{Volume})^{4/3}}{\min_{\alpha, \beta \in [0, 2\pi]} \iiint_{S(\alpha, \beta)} \max\{|x|, |y|, |z|\} dx dy dz} \quad (6)$$

where $S(\alpha, \beta)$ means that a shape S is rotated along the x-axis by α degrees, and along the y-axis by β degrees. These 3D shape descriptors were calculated from the scanned data of the four states described above in section 2.1.2.

In this research, the 1D shape memory properties were expanded to multi-dimensional ones. The multi-dimensional shape memory performance was calculated using the 2D and 3D shape descriptors. Like the tensile strain in a 1D shape memory test using the cyclic thermomechanical tensile test, the shape descriptors were normalized by the shape descriptor obtained from the original

(undeformed) shape. Then, new fixity and recovery ratios were defined for 2D and 3D deployment tests, as follows:

$$\text{Shape fixity ratio, } R_f = \frac{D_{n,f}}{D_{n,m}} \times 100 \quad (7)$$

$$\text{Shape recovery ratio, } R_r = \frac{D_{n,m} - D_{n,r}}{D_{n,m}} \times 100 \quad (8)$$

where $D_{n,f}$ is a normalized descriptor of a temporary shape, $D_{n,m}$ is a normalized descriptor of a deformed shape, and $D_{n,r}$ is a normalized descriptor of a recovered shape. The notation and formulae related to the multi-dimensional characterization are listed in Table 2-2.

Table 2-2 Multi-dimensional shape memory properties of SMP.

	1D	2D and 3D
Descriptor	Stain, $\varepsilon = \frac{l-l_0}{l_0}$	Normalized descriptor, $D_n = \frac{D-D_0}{D_0}$
Original shape	ε_0	$D_{n,0}$
Deformed shape	ε_m	$D_{n,m}$
Temporary shape	ε_f	$D_{n,f}$
Recovered shape	ε_r	$D_{n,r}$
Fixity ratio (%)	$R_f = \frac{\varepsilon_f}{\varepsilon_m} \times 100$	$R_f = \frac{D_{n,f}}{D_{n,m}} \times 100$
Recovery ratio (%)	$R_r = \frac{\varepsilon_m - \varepsilon_r}{\varepsilon_m} \times 100$	$R_r = \frac{D_{n,m} - D_{n,r}}{D_{n,m}} \times 100$

2.3. Multi-dimensional shape memory properties of SMPC

2.3.1. Thermomechanical and tensile properties of SMPC

DMA tests were conducted to investigate the thermomechanical properties of our SMPC. As shown in Figure 2-6, the storage modulus decreased sharply between 90°C and 130°C. The transition temperature was defined as the highest temperature of tangent delta (116.8°C and 121.6°C). When the temperature of the SMPC was higher than its transition temperature, the storage modulus was about 5 MPa and the SMPC was soft and readily deformable. Below its transition temperature, the storage modulus was about 4000 MPa, allowing the SMP to be fixed in a deformed shape after cooling. Considering that the high temperature exposed in the space environment reaches 120°C, the SMPC forms a suitable transition temperature that can be used in the space environment. Based on these results, cyclic thermomechanical tensile tests (Figure 2-8) and deployment tests were carried out between 30°C and 130°C.

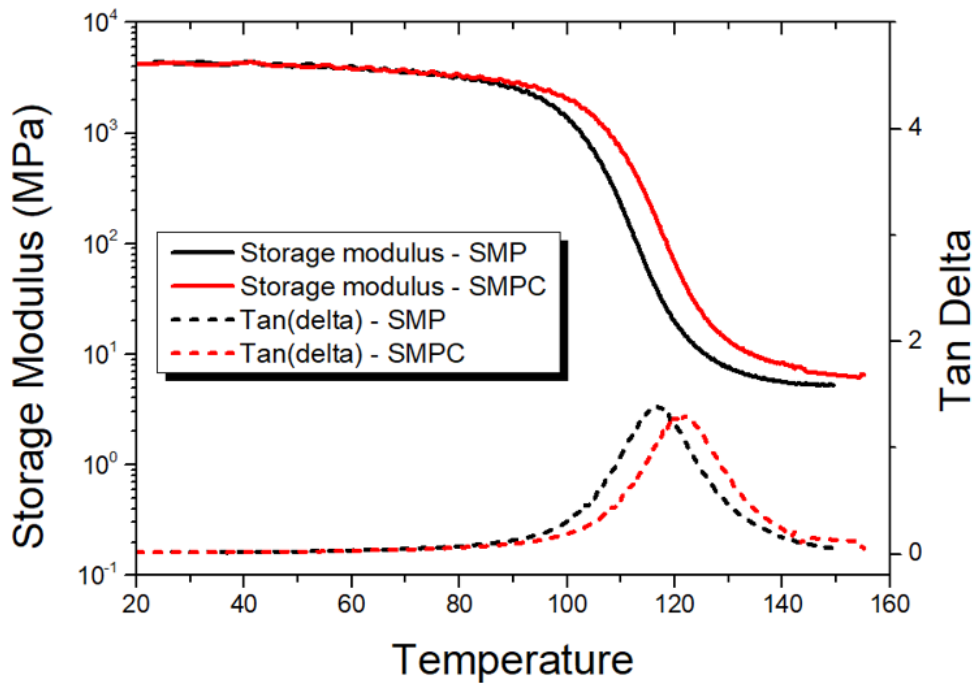
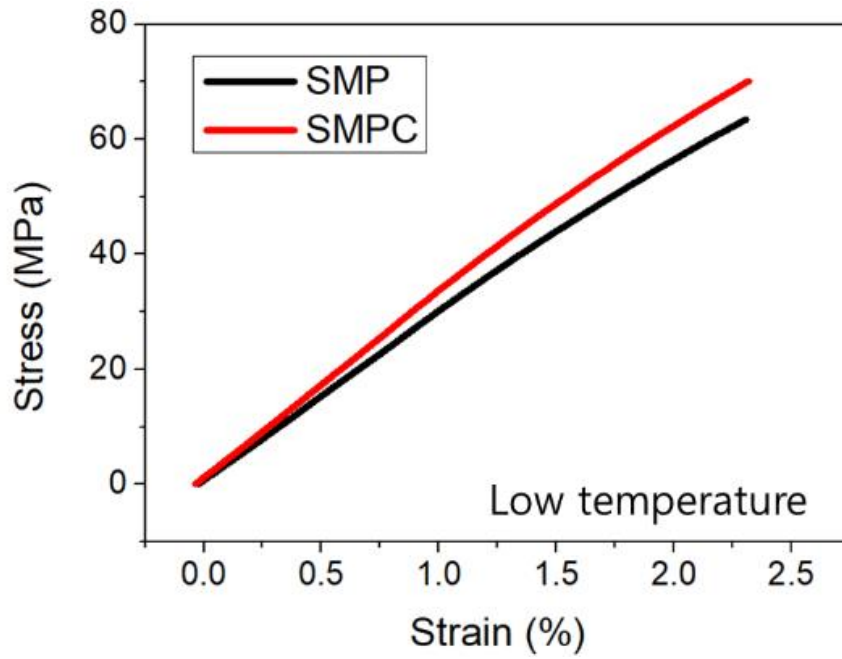
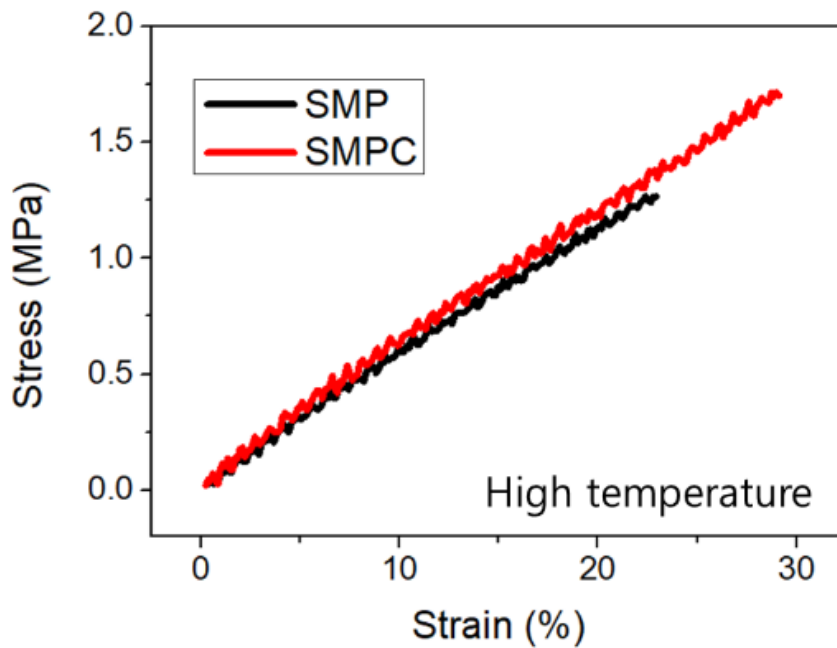


Figure 2-6 Thermodynamic curve of SMPC obtained using DMA.

From the tensile test results, the stress-strain curve and the tensile properties are shown in Figure 2-7 and Table 2-3. SMPC showed higher strength, rigidity, and elongation at break than SMP. Especially at higher temperatures above the transition temperature, the strength has increased to about 30%. It has been confirmed that it has better mechanical properties in a high temperature space environment.



(a)



(b)

Figure 2-7 Stress-strain curve of SMPC (a) below the transition temperature and (b) above the transition temperature

Table 2-3 Tensile properties of SMPC

	Young's modulus (MPa)		Tensile strength (MPa)		Elongation at break (%)	
	High temperature	Low temperature	High temperature	Low temperature	High temperature	Low temperature
SMP	9.58 (0.42)	2774 (97)	1.26 (0.17)	60.65 (3.42)	22.34 (2.95)	2.06 (0.22)
SMPC	10.03 (0.75)	2844 (121)	1.63 (0.18)	64.04 (7.44)	28.05 (4.00)	2.17 (0.36)

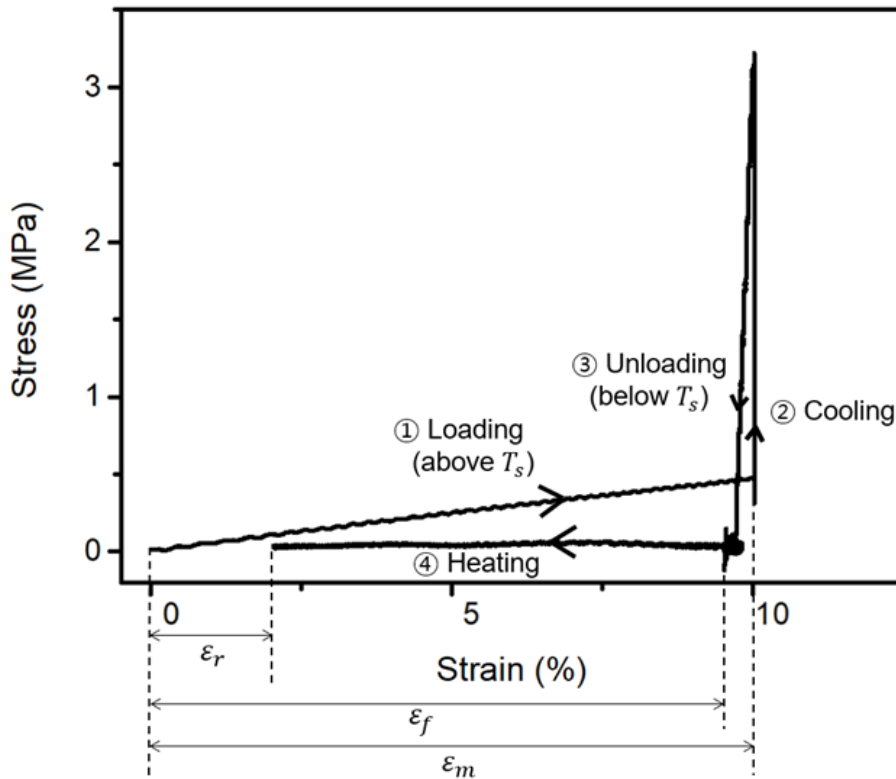


Figure 2-8 Cyclic thermomechanical behavior of SMP obtained using UTM.

The thermal properties of SMPC were characterized. The specific heat, thermal conductivity, and absorptivity of SMPC were measured and listed in the Table 2-4. The thermal conductivity of SMPC was expected to be higher than that of SMP, but it decreased slightly. In the case of electrical conductivity, when the CNT content exceeds the percolation threshold, it increases significantly, but it was not easy to increase the thermal conductivity due to the interfacial contact resistance between the CNT and the matrix. Since there is no heat transfer by convection in space, it was necessary to see how well the antenna could heat up by receiving solar radiation. The irradiance of the sun in a low orbit at an altitude of about 600 km appears as a blue graph in Figure 2-9. Most of the solar radiation energy is transmitted at wavelengths around 200 to 2000 nm. SMPs did not absorb radiation well. However, in the case of SMPC, the absorptivity was about 96%.

Table 2-4 Thermal properties of the SMP and SMPC

	SMP	SMPC
Specific heat at 30 °C (c_p , J/gK)	1.09	1.04
Thermal conductivity (λ , W/mK)	0.2159	0.2098
Absorptivity (%)	41.12	95.87

SMPC has a lower thermal conductivity than SMP, but its specific heat is small and its energy absorption rate is large, so it can absorb energy by solar radiation and raise the temperature of the material with less energy. As a result, the SMPC antenna can be deployed faster.

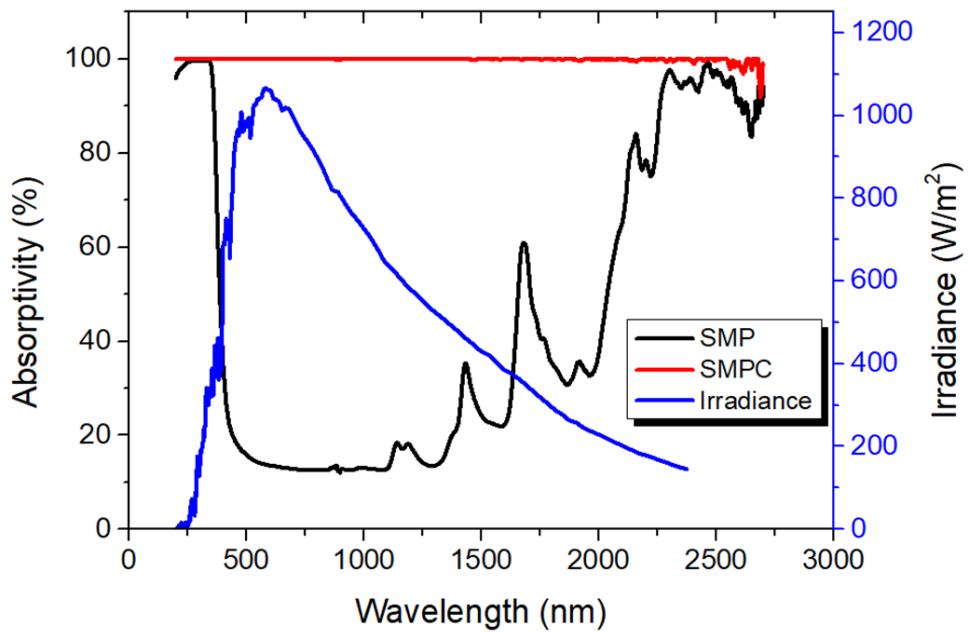


Figure 2-9 Absorptivity of SMPC and solar irradiance in low earth orbit

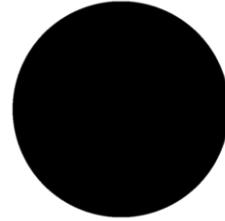
2.3.2. Multi-dimensional shape memory properties: comparison of 2D and 3D shape descriptors

We explored the effectiveness of 2D and 3D descriptors using a deployable 3D antenna model. For this, a virtual antenna was created using a 3D simulation program, COMSOL Multiphysics®. Park et al developed 3D constitutive equation to predict the deformation behavior of SMPs and implemented it into COMSOL Multiphysics® [96]. In the simulation, a virtual antenna, with a diameter of 150 mm and a thickness of 1.1 mm, was created. The folding process was conducted in the same manner as the real antenna was experimentally folded during the deployment test. From the simulation results, step-by-step 3D shape information of the antenna were extracted. The shapes adopted by the virtual antenna are shown in 오류! 참조 원본을 찾을 수 없습니다.(a)–(f). The obtained shapes underwent image processing as described in Figure 2-5. Table 2-5 shows the 2D and 3D shape descriptors calculated using this information.

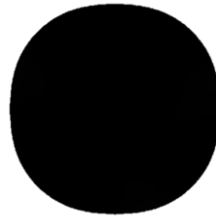
3D model

3D projected surface

(a)



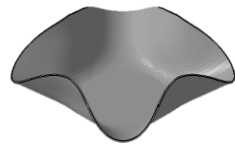
(b)



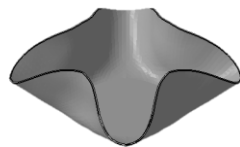
(c)



(d)



(e)



(f)



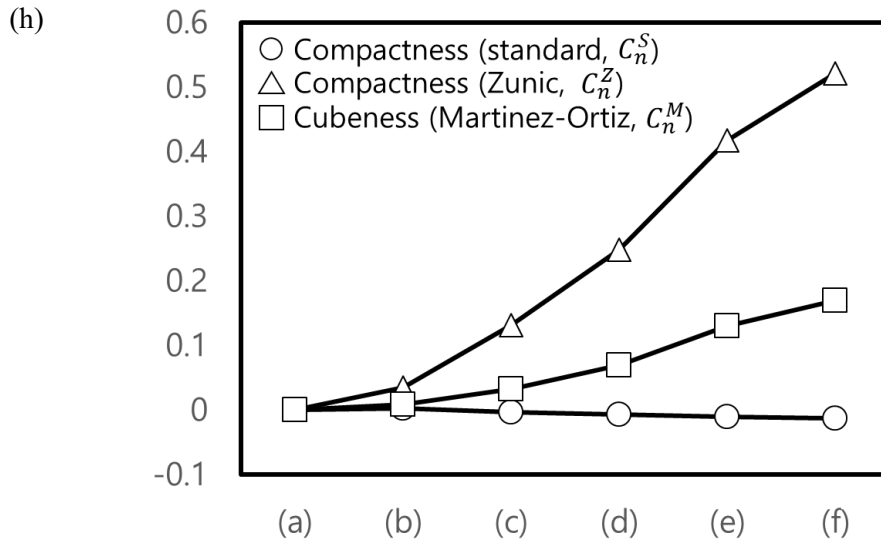
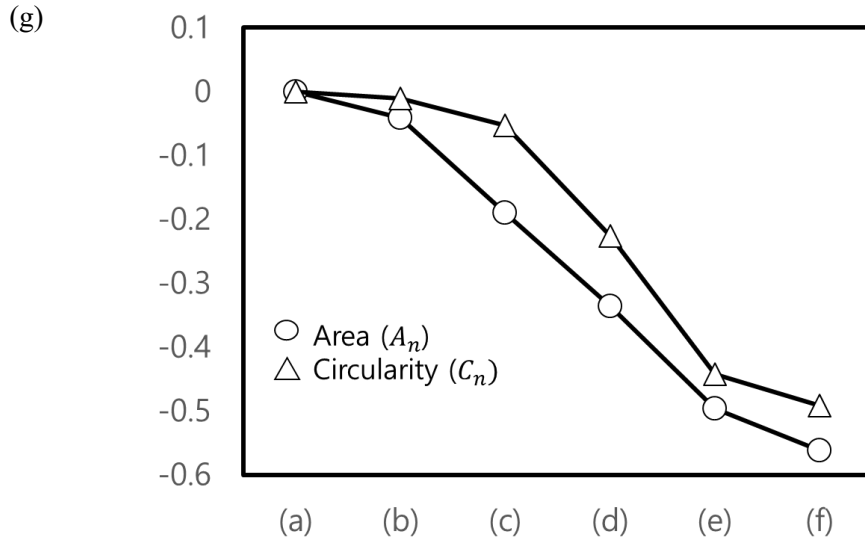


Figure 2-10 (a)–(f) 3D model and their 2D projected surface in the vertical direction, (g) 2D shape descriptors of the given shapes, and (h) 3D shape descriptors of the given shapes.

Table 2-5 2D and 3D shape descriptors of virtual antennas in figures 7(a)–(f).

Shape	2D						3D					
	Area (A , mm ²)	A_n	Circularity (C)	C_n	Compactness (C^s)	Angle (°)	Compactness (C^z)	C_n^s	Compactness (C^z)	Cubeness (C^M)	C_n^M	
(a)	17637	0	0.912	0	0.000434	0	0.02895	0.000434	0.1807	0		
(b)	16909	-0.0413	0.902	-0.0110	0.000435	22.7	0.02997	0.000435	0.1821	0.0083		
(c)	14300	-0.1892	0.864	-0.0526	0.000433	47.9	0.03274	0.000433	0.1865	0.0327		
(d)	11712	-0.3359	0.706	-0.2259	0.000431	64.8	0.03614	0.000431	0.1932	0.0699		
(e)	8887	-0.4961	0.509	-0.4419	0.000430	81.6	0.04104	0.000430	0.2042	0.1307		
(f)	7727	-0.5619	0.464	-0.4912	0.000429	90.0	0.04403	0.000429	0.2112	0.1695		

As the area and circularity of the antenna were maximal in the original shape (오류!

참조 원본을 찾을 수 없습니다.(a)), normalized values of these descriptors became negative (see Table 2-5) while the absolute values increased as the antenna was folded. From (a) to (c), the perimeter of the antenna was shortened. From (c) to (f), the perimeter was lengthened because the folded region started to become concave. The change in perimeter was smaller than the change in area, meaning that circularity is less sensitive to shape changes.

Note that compactness C^S is not solely suitable to describe the folding behavior of the antenna. Significant changes in surface area and volume yielded only slight changes in C^S . In contrast, the compactness C^Z increased substantially when the antenna was folded. The inverse of C^Z represents the sum of the dispersions of the object in the x-, y-, and z-axes [97]. Therefore, an increase in C^Z means that the dispersion of the 3D coordinates of the antenna gradually decreased, and the object became miniaturized or more compact. Finally, as the antenna was folded, its cubeness C^M increased, but at a rate lower than that of C^Z . As a result, 2D shape descriptors (area and circularity) combined with 3D compactness C^Z can adequately and numerically describe the antenna's folding behavior.

Other folded shapes were created in a 3D modeling program to evaluate the effectiveness of 2D and 3D shape descriptors. A virtual antenna with a 150 mm diameter and a 1.1 mm thickness was folded into (a) a 2-fold shape, (b) a 2-fold-2-layer shape, (c) a 4-fold shape, and (d) an 8-fold shape (see Figure 2-11). Table 2-6 shows the resulting 2D and 3D shape descriptors. The absolute value of the 2D shape

descriptor for the 2-fold shape was larger than that of the 2-fold-2-layer shape, meaning that the 2-fold shape change was larger than that of the 2-fold-2-layer shape. In contrast, the 3D shape descriptor of the 2-fold-2-layer shape was larger than that of the 2-fold shape. This is consistent with our perception, which means that the 2-fold-2-layer shape is more compact. Therefore, while the 2D shape descriptor is limited in describing changes in the z-direction, the 3D shape descriptor is able to better reflect the overall shape change of the antenna. In our perception, the 8-fold shape is more compact than the 4-fold shape in terms of packing. The volumes of the bounding box and convex hull of the 4- and 8-fold shape were calculated. Here, the bounding box and convex hull are a smallest-volume box and a smallest convex set, respectively, which completely enclose a given object. The volumes of the bounding box and the convex hull of 8-fold shape were 533 cm³ and 314 cm³, respectively, whereas those of 4-fold shape were 658 and 336 cm³. The values of 8-fold shape were smaller than those of 4-fold shape. The differences in 2D shape descriptors between the 4- and 8-fold shapes was small ($A_n = 13\%$, $C_n = 12\%$). However, the corresponding differences in the 3D shape descriptors were large ($C_n^Z=59\%$, $C_n^M =38\%$). The 3D shape descriptors showed the difference of the 4- and 8-fold shape more dramatically than the 2D shape descriptors.

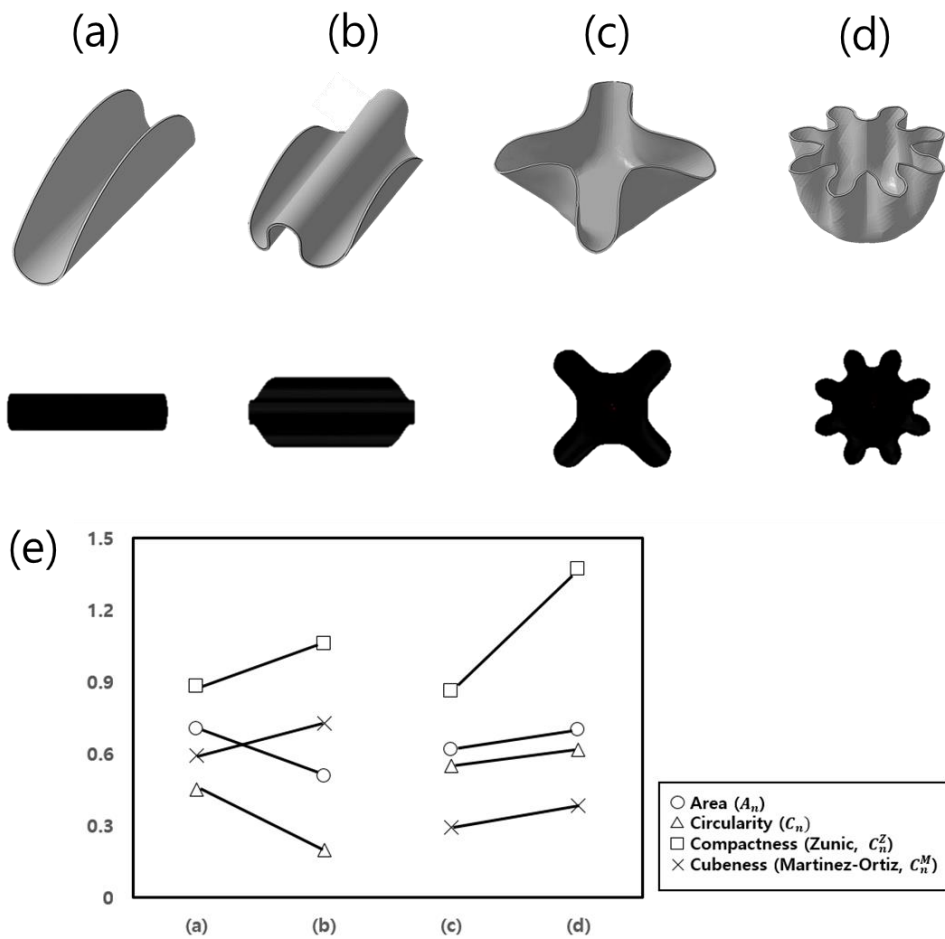


Figure 2-11 3D model and their 2D projected surface for comparison of 2D and 3D shape descriptors. (a) 2-fold model, (b) 2-fold-2-layer model, (c) 4-fold model, (d) 8-fold model, (e) 2D and 3D shape descriptors of the given shapes.

Table 2-6 2D and 3D shape descriptors of virtual antennas in figures 8(a)–(d).

Shape	2D			3D	
	Angle (°)	A_n	C_n	C_n^Z	C_n^M
(a)	-	-0.7046	-0.4516	0.8820	0.5920
(b)	-	-0.5065	-0.1980	1.0589	0.7288
(c)	90	-0.6185	-0.5506	0.8639	0.2918
(d)	90	0.7016	0.6162	1.3722	0.3833

2.3.3. Shape memory properties of deployable SMP

Figure 2-8 shows the results of the cyclic thermomechanical tensile test with our SMP. The 1D shape memory performance can be evaluated from the stress–strain curve. The stress–strain curve showed a similar tendency to the typical stress–strain curve (오류! 참조 원본을 찾을 수 없습니다.(b)). However, the stress was increased while the cooling process proceeded. It was because below the transition temperature the thermal expansion coefficient was negative for a stretched specimen so that the SMP contracted as the temperature decreased [48]. According to the equations (1) and (2), the fixity and recovery ratios were calculated. The fixity and recovery ratios were 98.0% (standard deviation = 0.2%) and 79.1% (standard deviation = 0.4%), respectively. Thus, this SMP was well-fixed into its temporary shape but was not able to completely return to its original shape.

After 3D deployment tests in 오류! 참조 원본을 찾을 수 없습니다., 2D and

3D shape descriptors of the SMP antenna were calculated based on the shape information of the four states: original, deformed, temporary and recovered shapes.

오류! 참조 원본을 찾을 수 없습니다. shows images obtained using the image analysis in Figure 2-5. According to the equations (7) and (8), the fixity and recovery ratio were calculated. The fixity and recovery ratio were nearly 100% (Table 2-7). Compared to those calculated from 1D shape memory parameters, the fixity ratio was reasonable but the recovery ratio was not. It seems that gravity helped the antenna recover its shape, resulting in complete recovery. In 1D shape memory tests, a 10% strain was applied evenly across the entire SMP specimen. However, in 3D deployment tests, the SMP antenna experienced strain only in the local region where the antenna folded. As such, the entire antenna was able to attain nearly 100% of its original shape, although the crumpled region did not return completely to its initial state. The 1D shape memory property did not accurately reflect the 3D deployment of the antenna. In contrast, 3D shape memory properties were successfully characterized by 3D shape descriptors, which were representative of whole changes in the antenna. The fixity ratio calculated using circularity differed only slightly from those of the other shape descriptors because circularity is based on the boundary of an image. Boundary-based descriptors are generally more sensitive to small shape changes. This also means, however, that these descriptors are vulnerable to noise, which can lead to undesirable results [98]. In contrast, area, compactness, and cubeness are area- or volume-based descriptors and are relatively insensitive to noise [98]. Therefore, area, compactness, and cubeness were suitable to describe the

deployment behavior of our SMP antenna.

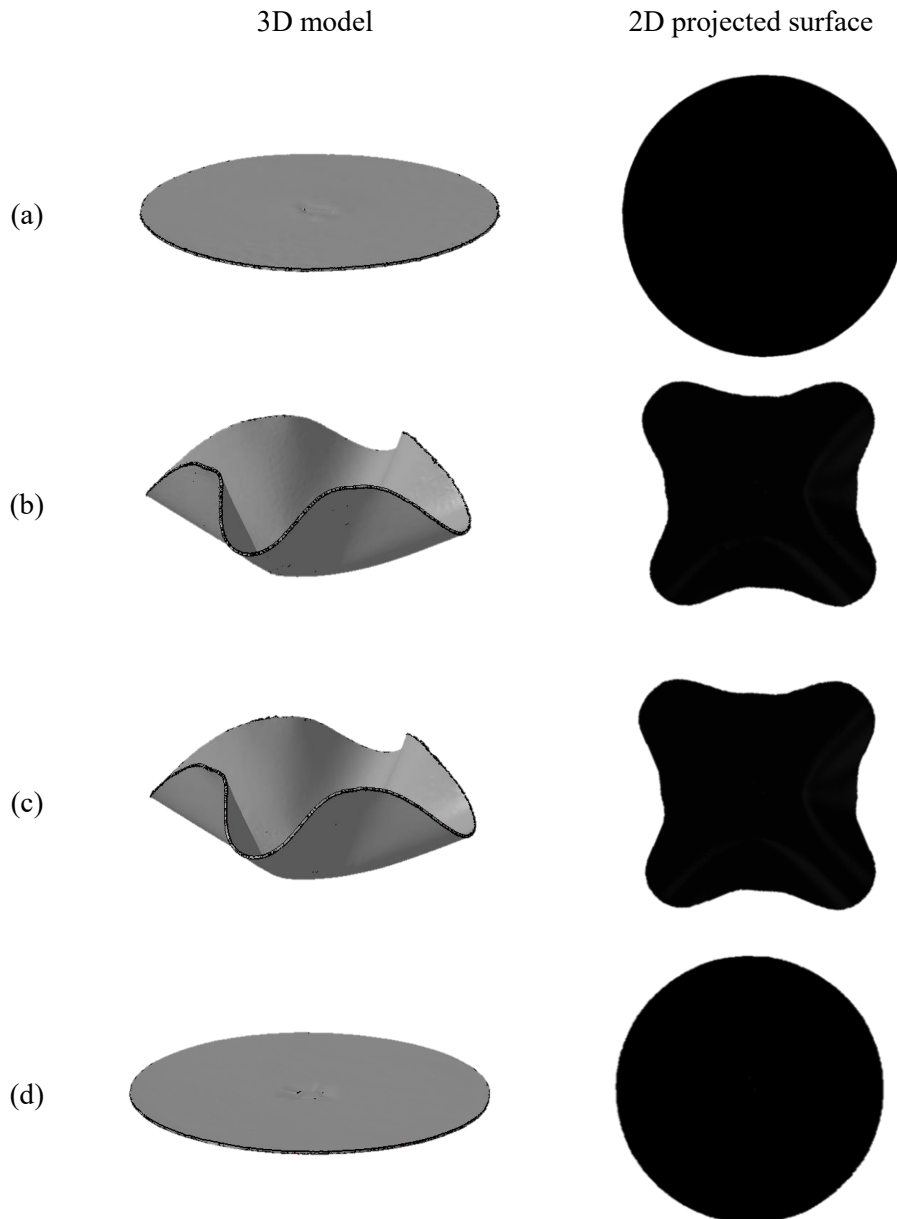


Figure 2-12 3D model of the SMP antenna during the deployment test, which was obtained by scanning its shape, and their 2D projected surface. (a) Original shape,

(b) deformed shape, (c) temporary shape, (d) recovered shape.

Table 2-7 3D shape memory properties of the SMP antenna.

Shape	2D				3D				$R_f(\%)^b$
	Angle ($^\circ$)	Area (A , mm 2)	C_n	Circularity (C)	A_n	Compactness (C^Z)	Cubeness (C^M)	C_n^M	
Original shape ^a	0	17838	0	0.900	0	0.02904	0.1811	0	
Deformed shape ^a	60.8	10571	-0.4074	0.663	-0.2633	0.04109	0.2056	0.1352	
*Temporary shape ^a	60.2	10579	-0.4069	0.671	-0.2544	0.04110	0.2056	0.1355	
*Recovered shape ^a	0.6	17720	-0.0066	0.897	-0.0033	0.02913	0.1811	0.0003	
	98.9 (0.2)	99.4 (0.4)		94.7 (1.6)		100 (0.2)	100 (0.1)		

$R_r(\%)^b$	99.2 (0.1)	99.1 (0.6)	95.7 (2.4)	99.5 (0.2)	99.3 (0.5)
-------------	---------------	------------	------------	------------	------------

^aThe shape descriptor values and normalized values are from one representative experimental data. ^bThe R_f and R_r are the average values from three experimental data and the values in parentheses are their standard deviations.

2.4. Summary

The 3D shape memory behavior of an SMP antenna was analyzed by introducing 2D and 3D shape descriptors. The 2D shape descriptors (area and circularity) were able to distinguish the 3D shapes of the SMP antenna, but were limited in detecting differences in compactness between shapes. Conversely, a new set of 3D shape descriptors, especially compactness C^Z , was able to accurately represent the 3D deployment behavior of the SMP antenna. Shape fixation and recovery ratios of the SMP antenna were quantified using this new set of 3D shapes, attaining values of 100% and 99.5%, respectively. These percentages differ significantly from those based on uniaxial strain. These data strongly validate the 3D shape descriptor for quantitatively describing the 3D deployment behavior of SMPs.

Chapter 3. 3D printing process of thermoplastic shape memory polymer composites

Pin-assisted Melt impregnation process was introduced to design a new 3D printing system. Melt impregnation is a conventional process used to fabricate CCFRTP preregs. Continuous carbon fiber bundles pass through a thermoplastic polymer melt in the impregnation bath, facilitated by various tools, such as w-shaped channels [102], fixed or rotational pins [103-105], and pins with radial slits or porous media [106-108]. In the pin-assisted melt impregnation process, the fiber bundle spreads as it passes between the pins, during which time the polymer melt diffuses and impregnates the fiber bundle. This process is very simple, requires only a small structure, and has good impregnation efficiency.

In this chapter, we propose a new 3D-printing method for CCFRTPs using a pin-assisted melt impregnation approach. The impregnation process was integrated with a 3D-printing system by designing an in situ pin-assisted melt impregnation head. The effects of varying printing conditions, i.e., of temperature, printing speed, layer height, degree of impregnation (DOI) of the printed composites, and the printability of the process, were investigated. Finally, tensile specimens were fabricated using the newly developed 3D-printing system and tested to verify impregnation uniformity and interfacial properties.

3.1. Preparation of a new 3D printing system

3.1.1. Design of the new printing system

Figure 3-1(a) shows a commercial 3D printer (Mark Two; Markforged Inc., USA) for printing CCFRTPs. Two print heads are used: one for printing nylon matrix filaments and the other for printing impregnated carbon fiber filaments. Note that the nylon matrix is printed in the same way as with a traditional fused deposition modeling (FDM) 3D printer. Since the process of impregnating continuous carbon fibers with nylon must be preceded, the printing process consists of two separate steps, i.e., impregnating and 3D printing. The in-nozzle impregnation 3D printer designed by Matsuzaki et al. [71] had a heating block with two entrances: one each for the matrix filament and carbon fiber roving (Figure 3-1(b)). There was a reservoir in the middle of the heating block, in which the carbon fiber was impregnated. The carbon fibers were impregnated as they passed through the heating block, and a CCFRTP composite strand was formed. After placing the composite strand on the building plate, the fiber and matrix were continuously extruded by moving the printing head. The matrix filament was fed according to the amount of matrix being extruded.

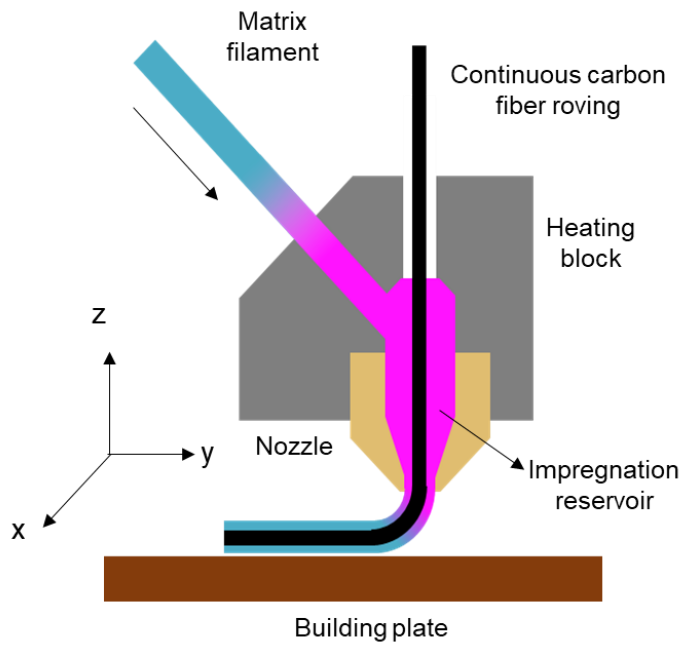
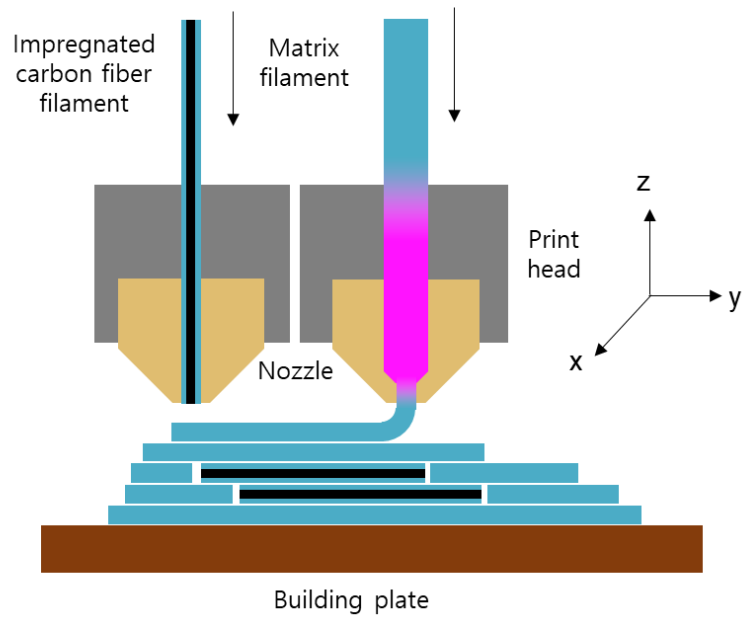
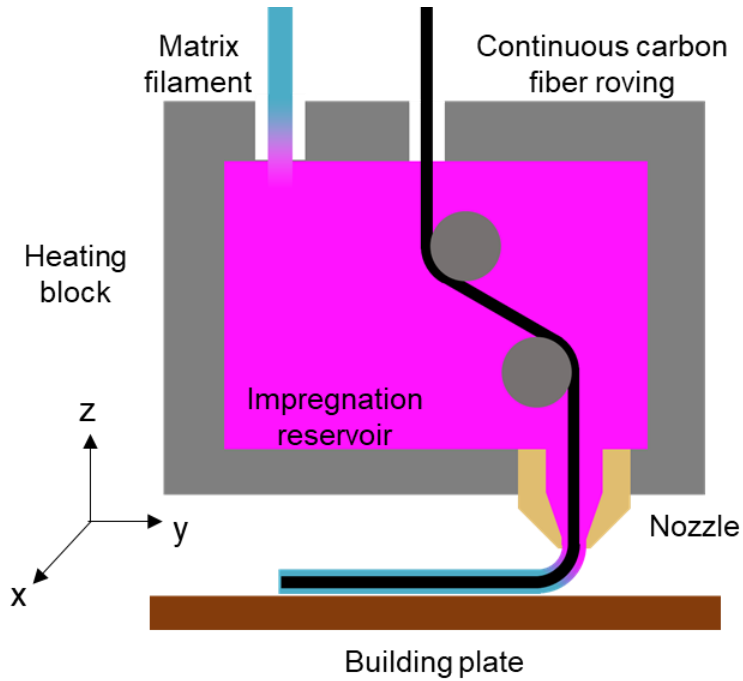
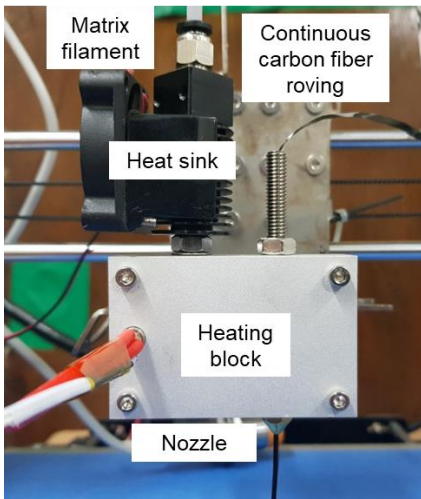


Figure 3-1 Previously developed 3D-printing system for CCFRPTs. (a) Commercial 3D printer (Mark Two [70]) and (b) in-nozzle impregnation 3D printer ([71]).

In this study, the printing head was modified by introducing *in situ* pin-assisted melt impregnation (Figure 3-2). This system also had two entrances, like the Matsuzaki in-nozzle impregnation 3D printer. The entrance for feeding the filament was heated to prevent the matrix material from clogging at the inlet. Note that a longer impregnation path was achieved using 3-mm-diameter pins in the heating block reservoir; this facilitated impregnation of the carbon fibers as they passed through the pins. This design was inspired by the melt impregnation process used to produce carbon fiber preregs with thermoplastic polymer matrices. With the help of the pins, more uniformly impregnated composite strands were printed on the building plate.



(a)



(b)



(c)

Figure 3-2 3D-printing system for CCFRTPs developed in this study. (a) Schematic illustration showing the *in situ* pin-assisted melt impregnation printing head, (b) actual printing system, and (c) inside of the heating block showing the pins.

3.1.2. Materials and printed samples

Three thermoplastic filaments were used as matrices in this research. Nylon filament (Markforged Inc.), polylactic acid (PLA) filament (Samdimall Co., Republic of Korea) and shape memory polyurethane (SMPU) filament (SMP Technologies Inc., Japan) were used as-received. Continuous carbon fiber dry roving (DowAksa İleri Kompozit Malzemeler San. Ltd., Turkey) composed of 3,000 single carbon fibers and carbon fiber filament (Carbon Fiber CFFTM; Markforged Inc.) composed of 1,000 single carbon fibers were used as reinforcements.

Nylon matrix and carbon fiber roving were used to evaluate the printability of the newly developed printer. CCFRTPs were printed under printing conditions varying in temperature, printing speed, and layer height. The number of fixed pins (0, 2, or 4) was varied to observe their effect on impregnation. Impregnation of nylon, PLA, and PU was conducted at 260°C, 230°C, and 215°C, respectively. The cylindrical composite strands were 1 mm in diameter and the volume fraction was 4.5%.

Printability was then evaluated based on the following criteria. First, the fibers must not be damaged when extruded from the nozzle. Second, the extruded composite must be well-seated on the printing bed. Third, the composite material must be printed with the intended shape. The DOI of the extruded composites was also measured to determine the capability of the newly developed printing system of CCFRTPs.

Tensile test specimens were prepared using Mark Two and in situ pin-assisted

nozzle-impregnation 3D printers. The specimens had dimensions of $100 \times 4 \times 1$ mm³. The specimens printed using the Mark Two instrument were composed of eight layers of nylon and six layers of carbon fiber filaments. The specimens printed by the in situ pin-assisted melt impregnation 3D printer were composed of two layers of composite strands. The carbon fibers were oriented in the longitudinal direction. The volume fraction of the composite filament was 4.5%.

3.1.3. Characterization

The thermal properties of the matrix materials were measured by differential scanning calorimetry (DSC; Discovery DSC; TA Instruments, USA) to identify the appropriate 3D printing temperature. The temperature range was set from 0°C to 250°C and the ramping rate was 10°C/min under a nitrogen gas atmosphere. The heat-flow curve was obtained after the second scan. The viscoelastic properties of the nylon were also measured using a rotational rheometer (DHR1; TA Instruments). Strain and frequency were 1% and 1 Hz, respectively, while the temperature was ramped from 200°C to 260°C.

The DOI was determined by polishing the cross-section of the composite strand, and then observing it by optical microscopy as follows [109]:

$$\text{Degree of impregnation (DOI)} = \frac{\text{Number of impregnated fibers}}{\text{Total number of fibers}}$$

where impregnated fibers refers to fibers for which at least half of the surface is

surrounded by a polymer matrix.

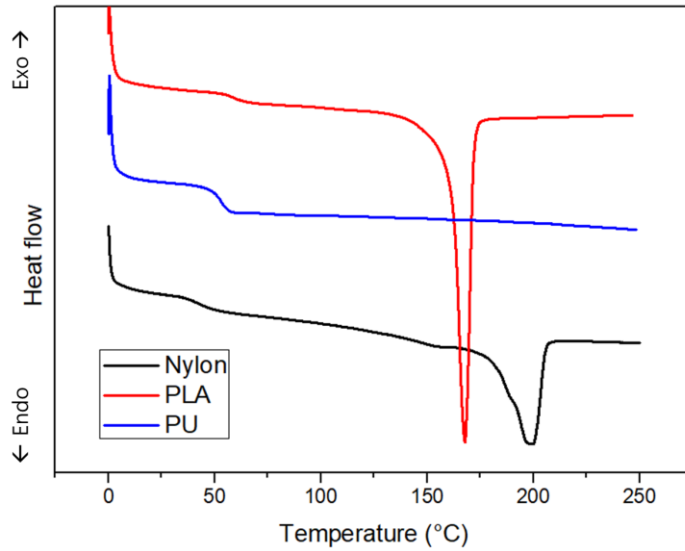
Tensile testing of the impregnated composite strands and 3D-printed composite tensile specimens was done using a universal testing machine (QUASAR 5; Galdabini, Italy). The gage length was 50 mm and the crosshead speed was 10 mm/min.

3.2. 3D printing of CCFRTPs

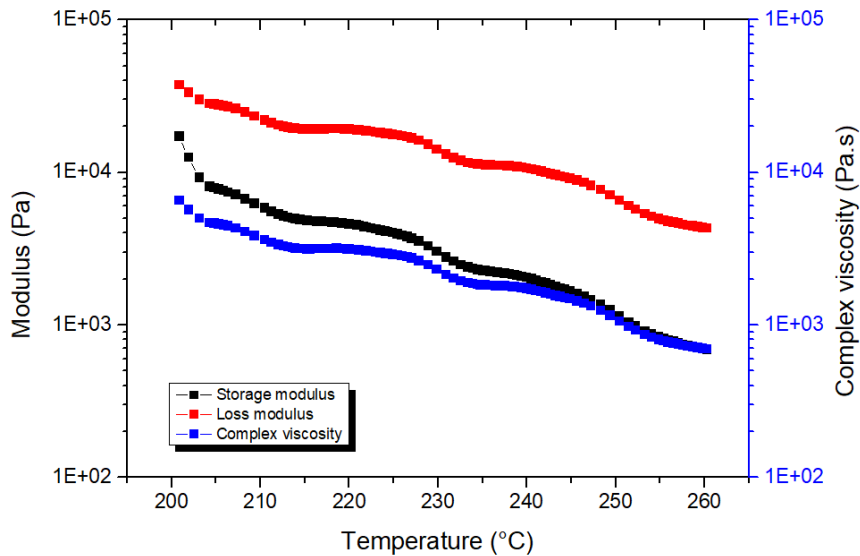
3.2.1. Printability of the new printing system

To identify the optimal printing condition, the thermal properties of the matrix filaments were first characterized. Figure 3 (a) shows the DSC curves of the nylon, PLA, and PU filaments. The nylon filaments displayed glass-transition and melting temperatures of 42°C and 200°C, respectively. The matrix should remain well-attached when printed on the building plate. Therefore, the temperature of the plate was set at 45°C, slightly higher than the glass transition temperature of the nylon, to improve adhesion. The temperature of the heating block was set at 260°C. The PLA filaments had glass-transition and melting temperatures of 56°C and 170°C, respectively. Hence, the temperature of the building plate was set at 60°C and that of the heating block at 230°C. The thermoplastic PU was composed of soft and hard segments. Its glass transition temperature, which corresponded to melting of the soft segments, was observed at 52°C. However, the melting temperature of the PU

filaments, which corresponded to melting of the hard segments, was not observed in the DSC thermogram. The temperature of the plate was set at 55°C and that of the heating block at 215°C, as recommended by the filament manufacturer.



(a)



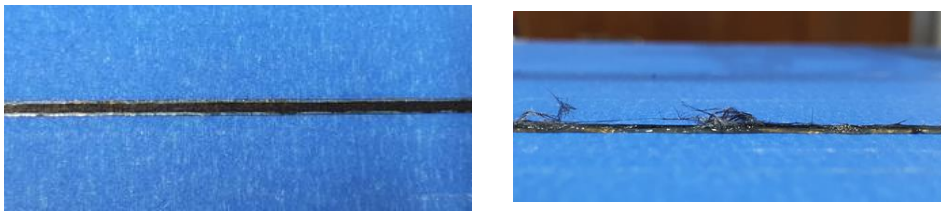
(b)

Figure 3-3 (a) Differential scanning calorimetry curves of the matrix filaments and (b) viscoelastic properties of the nylon filament.

Unlike the FDM process, the height of the CCFRTP layer printed by 3D printers is determined by the fiber thickness. The thickness of the tape-type carbon fiber roving used in this study was 0.08 mm, which established the minimum layer height as 0.08 mm. At a printing speed of 100 mm/min and heating block temperature of 260°C, printability was observed by changing the layer height from 0.1 to 1 mm (Table 3-1). The nozzle clogged and printing was impossible at layer heights less than 0.2 mm. Fibers were damaged by friction between the nozzle entrance and composite strand at layer heights between 0.2 and 0.4 mm (Figure 3-4(b)), but printing was possible at 0.5 and 0.6 mm (Figure 3-4(a)). At heights greater than 0.6 mm, the composite strand did not adhere to the build plate because of insufficient pressure to attach the strand to the building plate.

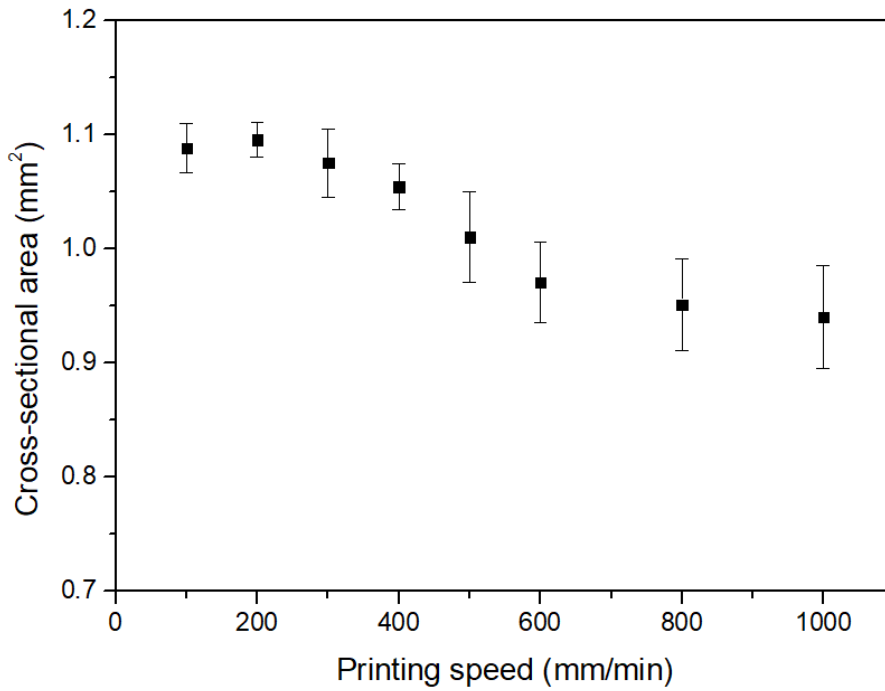
Table 3-1 Printability of CCFRTPs by the 3D printer using *in situ* pin-assisted melt impregnation under various printing conditions. Printability was classified as follows: the composite was printable (printable), the nozzle was clogged (clogged), the fiber was damaged or broken (damaged), or the composite strand was not attached to the build plate (not attached).

Layer height (mm)	Printing speed (mm/min)	Temperature (°C)	Printability
0.1			Clogged
0.2			Clogged
0.3			Damaged
0.4			Damaged
0.5	260	100	Printable
0.6			Printable
0.7			Not attached
0.8			Not attached
0.9			Not attached
1.0			Not attached
	100		Printable
	200		Printable
0.5	300	260	Damaged
	400		Damaged
	500		Damaged
	600		Damaged
		200	Not attached
0.5	100	220	Not attached
		240	Printable
		260	Printable



(a)

(b)



(c)

Figure 3-4 (a) Well-printed composite strand, (b) damaged composite strand, and (c) cross-sections of composite strands.

In an FDM 3D printer, the amount of polymer matrix extruded through the nozzle is determined by the speed at which the filament is supplied. The shape of a printed part is determined by controlling the amount of extrudate and the speed of the print head. This also applies to an in-nozzle impregnation 3D printer. However, in the *in*

situ pin-assisted melt impregnation 3D printer, the speed at which the filament is supplied does not affect the shape of the printed part because the distance between the inlet where the filament is supplied and the nozzle where the composite strand is printed is very large. The filament supply only replenishes the matrix material in the impregnation reservoir by the amount of matrix polymer that has been extruded. Thus, when the printed part does not adhere to the build plate, increasing the amount of matrix filament supplied does not result in attachment of the composite strand to the build plate. The amount and shape of the matrix to be printed are determined by the speed of carbon fiber roving, which is the same as the printing speed.

Composite strands were printed at various speeds to examine the relationship between the matrix amount and printing speed. With a 2-mm-diameter nozzle, the cross-sectional shape of the printed part should have been 2-mm-wide and 0.5-mm-thick. Figure 3-4(c) shows the cross-sectional area of printed composite strands as a function of printing speed. The cross-sectional area decreased with increasing printing speed. Generally, in the FDM process, the cross-sectional area of printed strands is inversely proportional to the printing speed. However, because the fibers are contained, the area no longer decreases above a certain printing speed. A printing area of 1 mm² was realized at a speed of 400–600 mm/min, although printing was still possible at speeds lower than 400 mm/min. Extruding a cross-section exceeding 1 mm² resulted in a lower extrusion rate due to pressure from adjacent strands. The observed printability (Table 3-1) confirmed that the composite strands were undamaged and printed well at speeds of 200 mm/min or less.

Printability was also observed as the temperature was increased above the melting point of the nylon filament (200°C). Increasing the temperature from 200°C to 260°C caused the viscosity of the nylon to gradually decrease from 6,640 to 700 Pa·s (Figure 3-3(b)). Lower viscosity corresponded to greater matrix fluidity, which facilitated placement on the build plate. Above 240°C, the composite strand was well-attached to the build plate, confirming its printability.

3.2.2. Degree of impregnation of the CCFRTPs

Figure 3-5(a) shows optical microscope images of nylon composite strand cross-sections. Small bright circles represent the cross-section of a single carbon fiber, and the dark material surrounding them corresponds to the nylon matrix. The inside of the region marked in red corresponds to the area where the fibers were not impregnated, and the outside area shows the impregnated region. The number of single fibers included in each area was counted using ImageJ software (NIH, USA). The total number of single fibers, i.e., 2,697, and the number of non-impregnated fibers, i.e., 1,737, corresponded to a DOI of 35.6%.

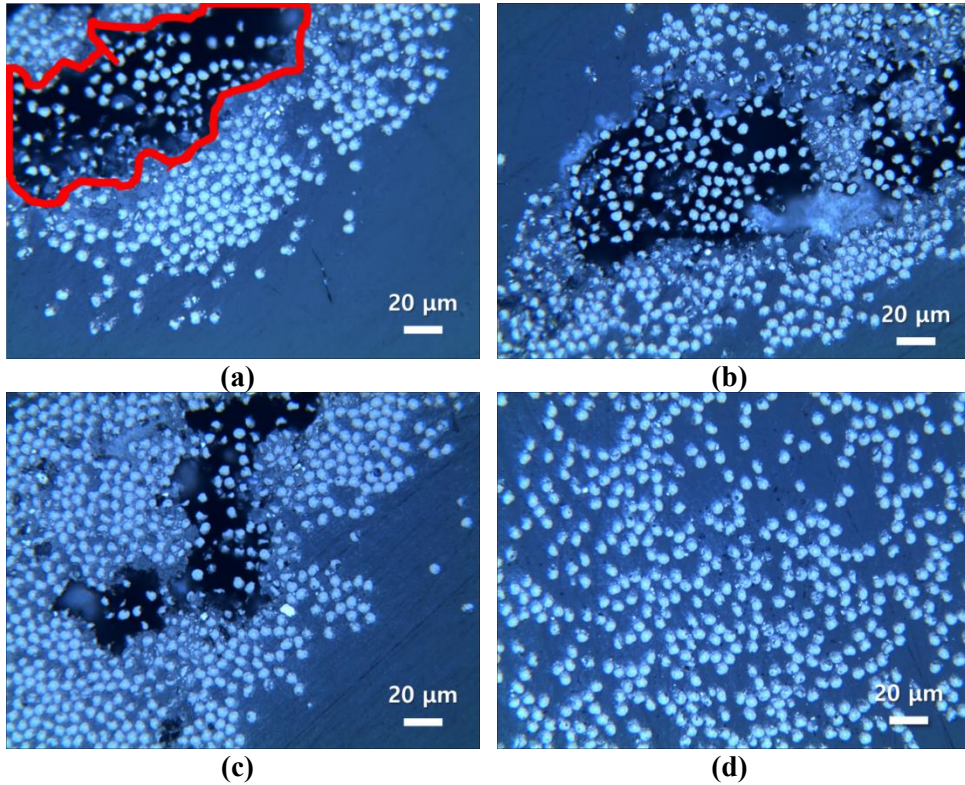
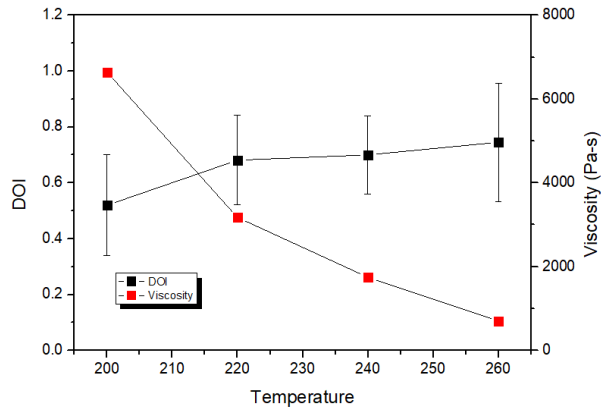


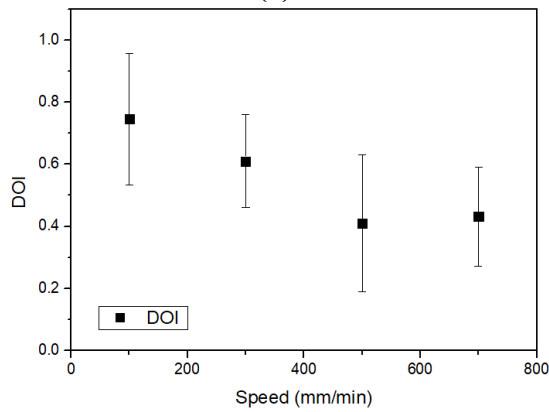
Figure 3-5 Cross-sections of nylon-impregnated composite filaments. (a) Impregnated and non-impregnated regions using (b) 0, (c) 2, and (d) 4 pins.

The melt impregnation behavior of the carbon fiber roving can be explained by diffusion of fluid into the porous medium. According to Darcy's law, the depth at which a fluid penetrates into a medium is inversely proportional to the viscosity of the fluid [78]. In the melt impregnation process, the DOI is inversely proportional to the square root of the viscosity [110]. Figure 3-6(a) shows that the DOI increased as the viscosity of the nylon decreased with increasing temperature. The viscosity decreased by 89% but the DOI did not increase significantly. The DOI of the composite decreased slightly with increasing printing speed (Figure 3-6(b)). Figure

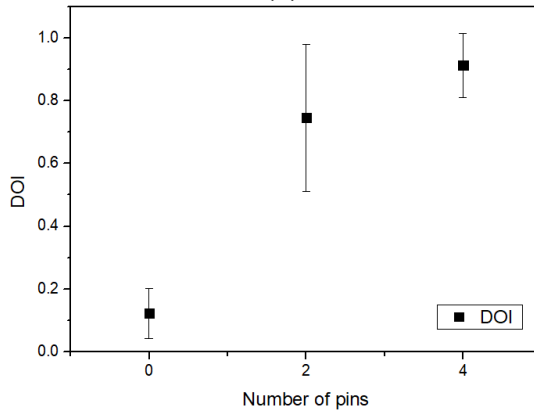
3-5(b)~(d) shows cross-sections of composite strands fabricated by in situ melt impregnation using 0, 2, and 4 pins, respectively. Especially when the composite was printed using four pins, the single fibers were well-dispersed and well-impregnated with matrix. The DOI increased with increasing number of pins (Figure 3-6(c)). The nylon composite printed by in situ melt impregnation using four pins had a DOI of 91.2%. A similar DOI (94.5%) was achieved when four pins were used with impregnated carbon fiber filament. The printed specimens were expected to have good mechanical properties.



(a)



(b)



(c)

Figure 3-6 Relationship between the (a) temperature and degree of impregnation (DOI) (printing speed = 100 mm/min; number of pins = 2), (b) printing speed and DOI (printing temperature = 260°C; number of pins = 2), and (c) number of pins and DOI (printing temperature = 260°C; printing speed = 100 mm/min).

3.2.3. Mechanical properties of the CCFRTPs

According to the printability and DOI results obtained under various printing conditions, the optimal printing conditions were identified as follows: printing speed of 100 mm/min, heating block temperature of 260°C, and layer height of 0.5 mm. To investigate the effect of pins on the printing behavior, 0, 2, and 4 pins were used. Furthermore, two commercial printers (Mark Two and in-nozzle impregnation 3D printers) were used for comparison purposes. Figure 3-7 shows the tensile test results of the printed nylon composite strands. The continuous carbon fiber-reinforced nylon composite exhibited better mechanical properties than those printed from nylon only. As the number of pins increased, the tensile strength, elastic modulus, and breaking strain increased due to improved impregnation. When two pins were used, the carbon fiber broke at about 2–2.5% strain and pull-out occurred, after which the nylon matrix around the carbon fiber became elongated; the tensile behavior of pure nylon was similar. In the four-pin case, the interfacial properties were improved, which resulted in failure of the matrix at about 5% strain.

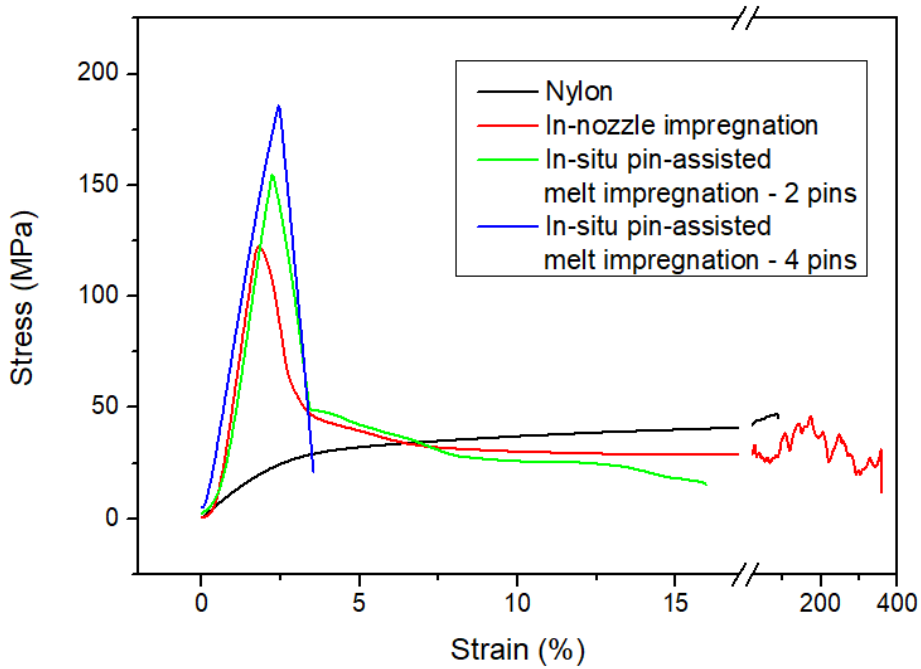
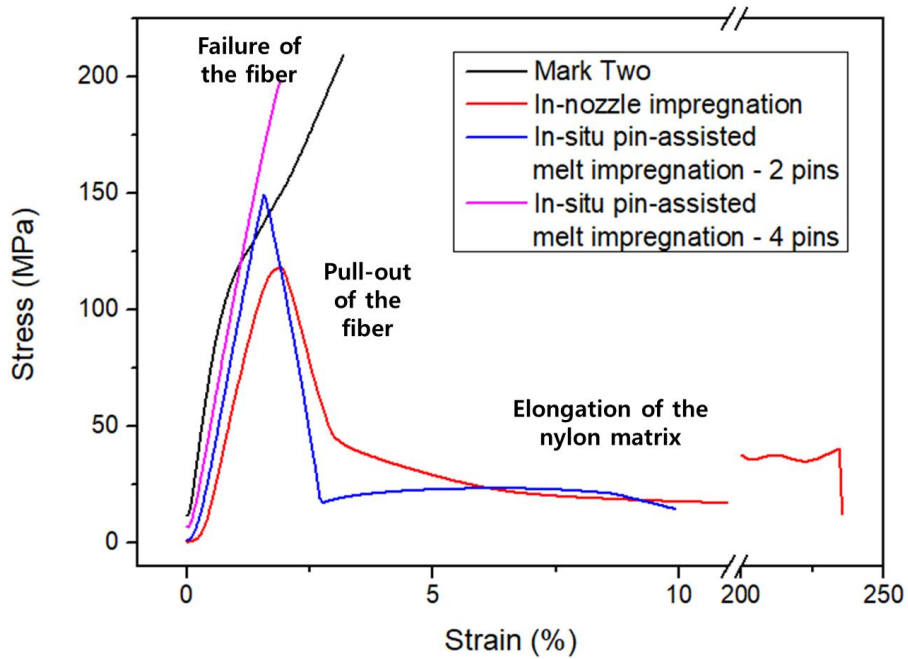


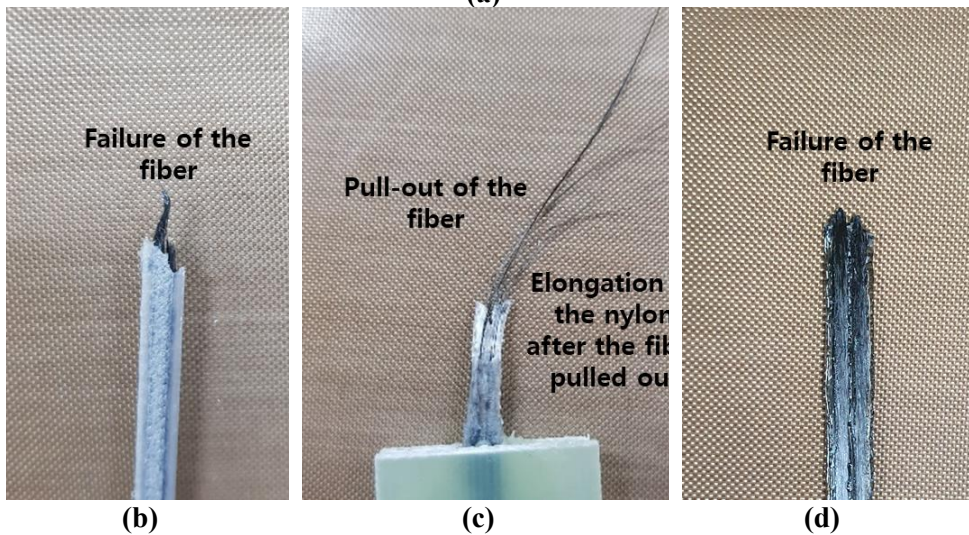
Figure 3-7 Tensile test results of the nylon-impregnated composite strands.

Figure 3-8(a) shows the tensile test results of the 3D-printed nylon composite tensile specimens (length \times width \times thickness = 100 mm \times 4 mm \times 1 mm). The specimen printed by the Mark Two printer had the highest tensile strength. The printed composite strands, and those printed by the pin-assisted melt impregnation 3D printer, behaved similarly, i.e., their mechanical properties improved with increasing number of pins. Notably, specimens printed using four pins had a tensile strength and elastic modulus comparable to those of the Mark Two-printed specimens. Specimens printed using the in-nozzle impregnation 3D printer with two pins displayed pull-out of fibers from the matrix and elongation of the nylon matrix due

to poor impregnation of the fibers (Figure 3-8(b)). However, failure of specimens printed using four pins, and with the Mark Two printing system, occurred at low strain due to a high DOI (about 90%). Specimens fractured simultaneously upon fiber breakage (Figure 3-8(a) and (c)).



(a)



(b)

(c)

(d)

Figure 3-8 (a) Tensile test results of the 3D-printed tensile specimens. Failure of 3D-printed tensile specimens printed by the (b) Mark Two printer, (c) in-nozzle impregnation 3D printer, and (d) *in situ* pin-assisted melt impregnation 3D printer equipped with four pins.

Fused deposition modeling has the disadvantage of weak interlayer bond strength. However, in the case of continuous fiber-reinforced composites, weakening of the interlayer bonding has no significant effect because the fibers are reinforcing in the tensile direction. The 3D-printing process with continuous fiber-reinforcement has the advantage that fibers can be oriented in the direction of the external force. However, with the in-nozzle impregnation 3D printer, the interfacial bonding between the fiber and the matrix was weak, so the reinforcing effect was less than expected. The impregnation and interfacial properties were improved using the new 3D printer design, which resulted in a strong reinforcing effect by the carbon fibers.

Table 3-2 shows the tensile test results of the 3D-printed CCFRTPs composed of various materials. The PLA and SMPU composites were printed under identical conditions; only the matrix materials were changed. The mechanical properties of the composites improved with increasing number of pins. By integrating impregnation and 3D-printing processes, our design provides users with the ability to select matrix polymers and fibers depending on the application.

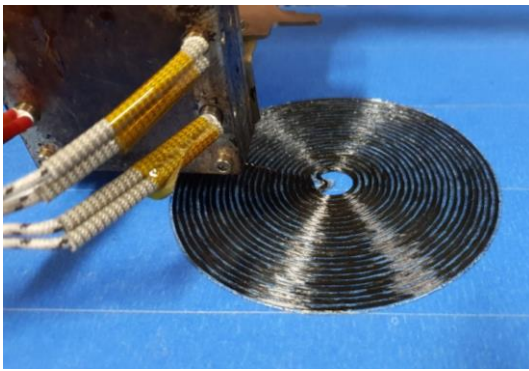
Table 3-2 Tensile properties of CCFRTPs made with various matrix materials 3D-printed by the *in situ* pin-assisted melt impregnation 3D printer.

Specimen		Tensile strength (MPa)	Young's modulus (MPa)	Elongation at break (%)
Nylon composites	In-nozzle impregnation	152	8051	253.0
	<i>In situ</i> pin-assisted			
	melt impregnation - 4 pins	189	11723	2.61
PLA composites	In-nozzle impregnation	221	7766	2.01
	<i>In situ</i> pin-assisted			
	melt impregnation - 4 pins	252	12883	3.95
SMPU composites	In-nozzle impregnation	228	7766	6.12
	<i>In situ</i> pin-assisted			
	melt impregnation - 4 pins	311	11090	7.52

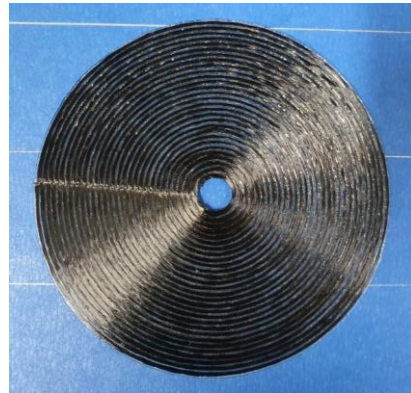
3.3. 3D printing and 3D characterization of SMPCs

Using the 3D printer, a miniature of the SMPC reflector antenna was printed with one layer, thickness of 0.6 mm, and diameter of 130 mm (Figure 3-9(a)). Using the folding device mentioned in Chapter 2, the deployment behavior was observed. The carbon fiber reinforced SMPC had an elongation at break of 7.52% and did not deform well. Since the folding device folds the antenna while the arms in the radial direction are folded, the carbon fiber direction of the antenna was arranged in the direction that the carbon fibers mainly received bending stress. That is, the carbon fiber was printed as it concentrically extending outward from the center of the

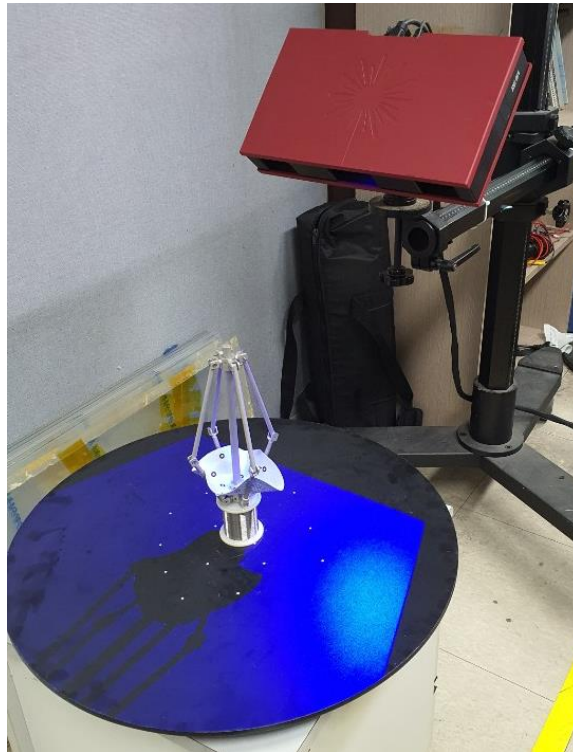
antenna (Figure 3-9(b)).



(b)



(c)



(c)

Figure 3-9 (a) 3D printing of SMPC antenna, (b) 3D printed SMPC antenna, and (c) 3D scanning of the deployment process using 3D scanner.

The deployment behavior of the antenna was scanned by a 3D scanner (Figure 3-9(c)). The antenna was deformed at 100°C, cooled to room temperature, and removed from the folding device to form temporary shape. Then, it was heated to 100°C again to restore the original shape. During the deployment process, the original shape, deformed shape, temporary shape, and recovered shape were scanned to get 3D shape information (Figure 3-10). The shape memory properties characterized by compactness and it was shown in Table 3-3. The shape fixity ratio was 85.8% and the shape recovery ratio was 64.2%. The printed composite material had high fixity ratio due to the stiffness of the carbon fiber. However, since the antenna was printed as a single layer, the SMP matrix between the carbon fibers were fractured because of the bending stress so that the shape cannot recover its original shape completely.

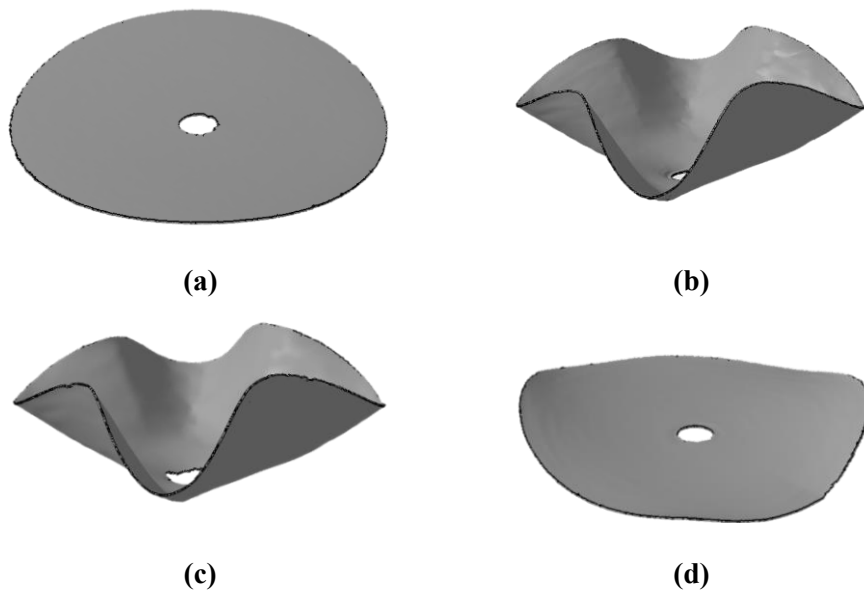


Figure 3-10 The 3D scanned image during the deployment test. (a) Original shape, (b) deformed shape, (c) temporary shape, and (d) recovered shape.

Table 3-3 Shape memory properties of SMPC antenna.

Shape	Compactness (C^Z)	C_n^Z
Original shape	0.0315	0
Deformed shape	0.0421	0.3365
Temporary shape	0.0406	0.2889
Recovered shape	0.0353	0.1206
$R_f(\%)$	85.8	
$R_r(\%)$	64.2	

3.4. Summary

A new 3D-printing system for CCFRTPs was developed by introducing pin-assisted melt impregnation to an FDM-type 3D printer. This new method features an integrated one-step process, in which the impregnation and printing processes proceed simultaneously. Printability was evaluated by considering whether the CCFRTP printed well in the desired shape, if the fibers and matrix were damaged, and if the printed part was well-attached to the build plate. The DOI was also investigated by varying the printing conditions. Improved impregnation increased the reinforcing effect of the carbon fiber. Although the device has a much lighter and simpler structure than other CCFRTP printing processes, the mechanical properties of the printed CCFRTP were comparable to those from a commercial 3D printer. The developed printing system enables the user to select the polymer matrix and reinforcing fiber, while effective in situ pin-assisted impregnation enables these choices to be easily changed. Finally, using the 3D printer, an SMPC antenna was successfully printed and the 3D shape memory properties were characterized using shape descriptors.

Chapter 4. 3D printing process of thermosetting shape memory polymers

The usual 3D printing methods for thermosetting polymers have disadvantages that they need long post-curing process and they cannot print free-standing structure without supporting materials. To overcome the shortcomings, a 3D printing method for thermosetting polymers using frontal polymerization has been studied [111]. A schematic illustration of the frontal polymerization used in 3D printing is shown in Figure 4-1(a). The monomer solution is prepared and incubated to make it rheologically suitable for 3D printing. Some of the monomers react and turn into oligomers and become a gel state capable of 3D printing. Radical-based frontal polymerization begins with local irritation such as heat or light sources to the gel state solution. This stimulation activates the catalyst, creating a high concentration of radical intermediates in the local area. During the polymerization process starting from the intermediates, exotherm occurs, and the heat locally raises the temperature of the nearby solution. The catalyst is activated by the elevated temperature, and the chain of processes aforementioned is repeated [112]. As a result, the polymerization proceeds “frontally.” The polymerization is very fast and energy efficient. If the frontal polymerization is used for 3D printing, it is possible to 3D print a free-standing structure directly without any supporting materials because the 3D printed filament is polymerized and retains its shape before it collapses. The use of free-standing structure can increase the complexity of geometric shapes, which expanding

the use of SMP.

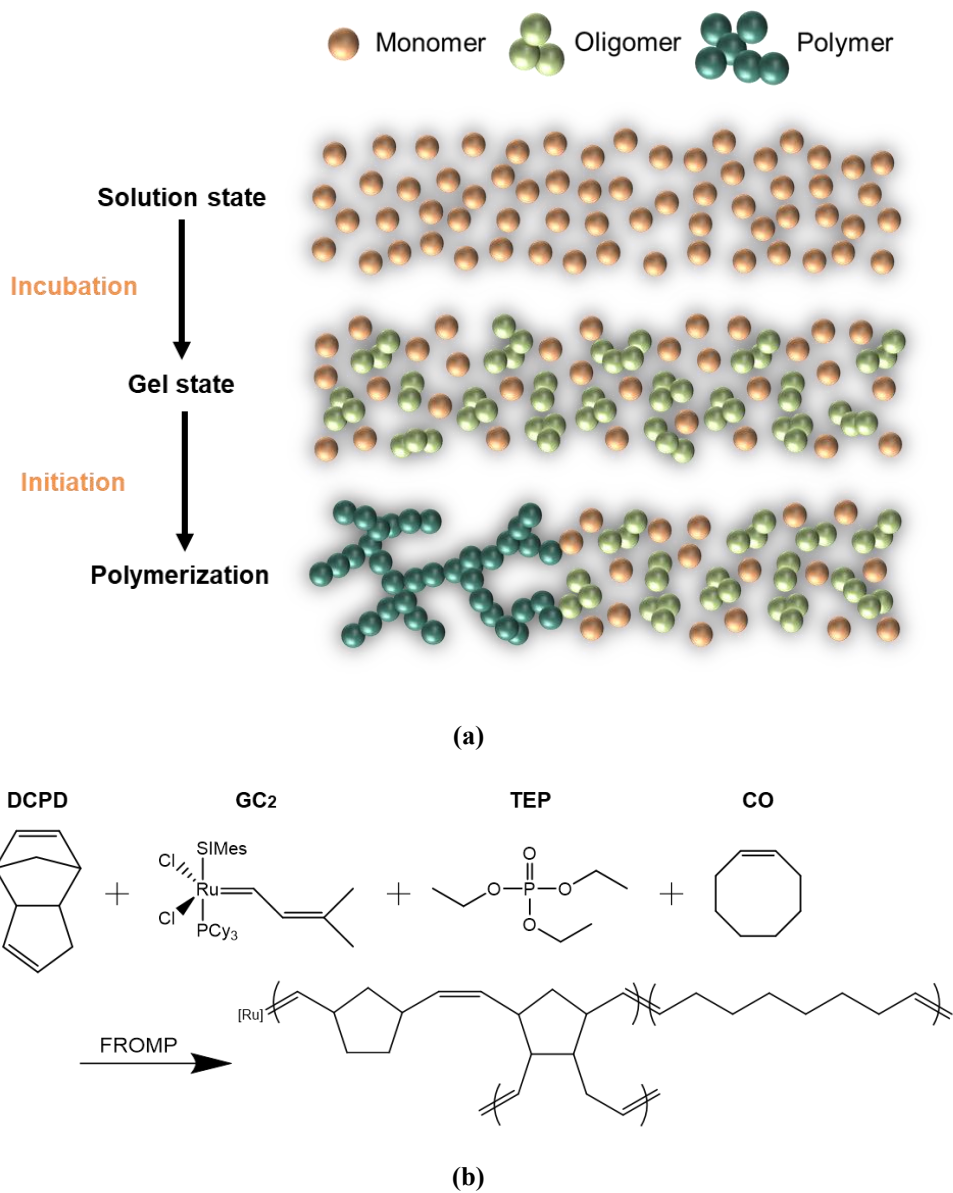


Figure 4-1 (a) Schematic diagram of frontal polymerization and (b) polymerization mechanism and chemical structure of frontal SMP.

In this chapter, a thermosetting SMP capable of frontal polymerization was prepared. The method of polymerizing dicyclopentadiene (DCPD) using Grubbs' catalyst is a well-known frontal polymerization method. Here, cyclooctene was polymerized together to make a polymer showing shape memory behavior (Figure 4-2(b)). The thermodynamic properties and the shape memory properties of SMP were measured. In addition, for use in 3D printing, the rheological properties and the speed of frontal polymerization were analyzed. Based on the rheological properties and frontal velocity, 3D printing conditions were determined. A 3D structure was printed to demonstrate that it is possible to print a free-standing structure. Finally, the shape memory behavior of the 3D printed SMP was observed and evaluated.

4.1. Preparation of a new 3D printing system

4.1.1. Materials and sample preparation

DCPD, *cis*-cyclooctene (CO), 5-ethylidene-2-norborene (ENB), 2nd generation Grubbs' catalyst (GC2), phenylcyclohexane (PCH) and triethyl phosphate (TEP) were purchased from Sigma-Aldrich. It was used as received without any purification process. Since DCPD exists as a solid at room temperature, it was melted at 50°C and then 5 wt% of ENB was added to depress the melting point. In this composition, DCPD solution existed in a liquid state at room temperature. Then, a DCPD/CO solution was prepared by adding CO in an amount corresponding to 0, 0.15, and 0.3 relative to the molar equivalent of DCPD, and then mixed for 5 minutes

at 2000 rpm through a planetary centrifugal mixer (ARE-310, Thinky corporation, Japan). In the case of the catalyst solution, GC2 in an amount corresponding to 100 ppm of the DCPD/CO solution was mixed with PCH and TEP (phosphate inhibitor) in an amount of corresponding to 100 molar equivalents of GC2 was added. After that, it was mixed for 5 minutes at 2000 rpm through the planetary centrifugal mixer. The DCPD/CO solution and the catalyst solution were further mixed for 1 minute at 2000 rpm through the planetary centrifugal mixer, followed by degassed at 2200 rpm for 1 minute. The final solution is the ink for 3D printing.

4.1.2. Characterization

4.1.2.1. Thermomechanical and shape memory properties

Thermal analysis was conducted through thermogravimetric analyzer (TGA, Discovery TGA, TA instruments, USA) to confirm whether the DCPD/CO copolymer was formed well. The temperature range was from room temperature to 600°C, and a heating rate was 10°C/min in a nitrogen atmosphere. Then, thermomechanical properties and shape memory performance were measured using dynamic mechanical thermal analysis (DMA, DMA Q800, TA instruments, USA). All properties were measured through tensile mode. Thermomechanical properties (glass transition temperature and storage modulus) were measured at a temperature range of 0°C to 150°C with a heating rate of 5°C/min, and a frequency of 1Hz through a multi frequency-strain module. In the case of shape memory performance, the

commonly used one-dimensional characterization method was used [6, 113]. The DMA strain module was used, and the temperature of the fixing step was set to 25°C, the temperature of the recovery step was set to 100°C, and the strain was set to 10%. The detailed shape memory performance measurement process was described in section 4.2.1.

4.1.2.2. Measurement of rheological properties and frontal velocities

The ink for 3D printing was incubated at 25°C so that it could have rheological properties capable of 3D printing. The rheological properties of the ink varying with the incubation time were measured using a rheometer (AR2000, TA instruments, USA). A 20 mm, 1° steel cone was used, and the test was conducted with a frequency of 1Hz and strain of 0.1% at 25°C. In addition, the ink was put into a syringe of the 3D printing system, and the extrusion was observed according to the incubation time while extruding at a rate of 0.147 mL/min.

To measure the frontal velocity of the ink, the ink was placed in a cylinder with an inner diameter of 6.5 mm and a length of 72 mm. A local point of the ink was heated by a soldering iron. During the frontal polymerization, the temperature change was observed using an IR camera (FLIR A320, FLIR Systems, USA), and the frontal velocity was calculated.

4.1.3. 3D printing process

For 3D printing, the ink was put into a 6 mL syringe, and incubated at 25°C until printing was possible. Then, the syringe was placed in a cooling chamber maintained -5°C to delay the rate of gelation. The printing head was installed in a 3D plotter of a 3D printer (Pinter 300, Samdimall Co., Republic of Korea). The printing head extruded the ink at a constant rate and printed the ink on the build plate. By heating with a soldering iron at a distance of 10 mm from the end of the nozzle, frontal polymerization was initiated to fix the shape of the printed product.

4.2. 3D printing of the thermosetting SMP

4.2.1. Thermomechanical and shape memory properties

DCPD is a representative monomer of thermosetting polymer in which polymerization occurs through ring-opening metathesis polymerization (ROMP). Ruthenium-based catalyst is mainly used in this reaction and a typical ruthenium-based catalyst is Grubbs' catalyst. When thermal stimuli is applied, a self-propagation and polymerization occurs [41]. CO is also a representative monomer of thermoplastic polymer that undergoes ROMP using a ruthenium catalyst [114, 115]. When CO is added to DCPD solution, the polymerization reaction of DCPD and CO occurs at the same time, forming a copolymer [116, 117].

Thermogravimetric analysis was conducted to confirm the thermal stability

according to the CO content (Figure 4-2). As the molar equivalent of CO increases, it began to decompose at a lower temperature. This was because CO has a linear chain structure when polymerization occurred, so it was more vulnerable to temperature [118].

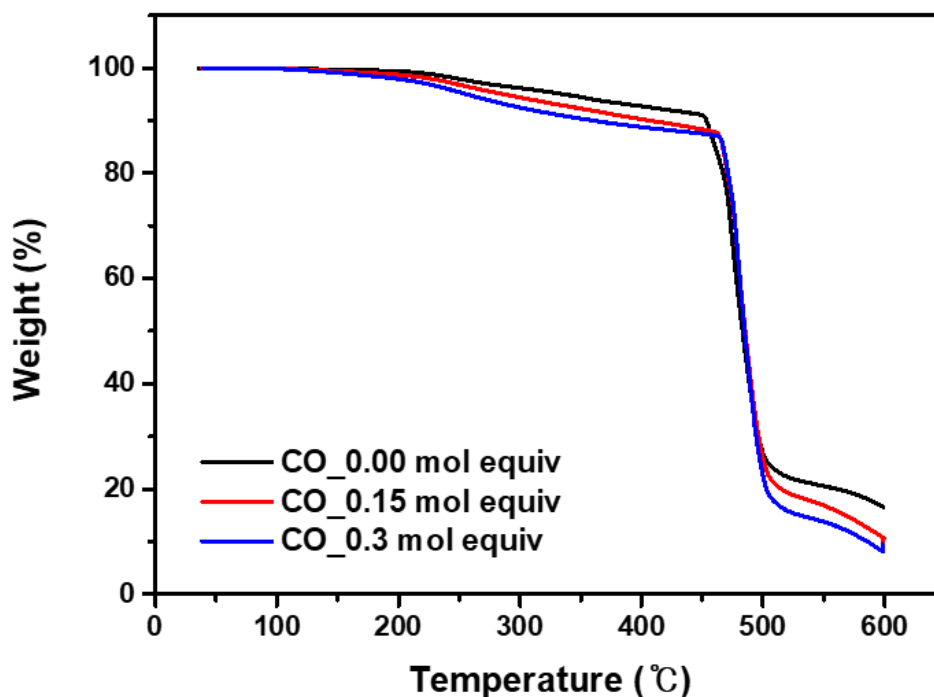


Figure 4-2 TGA analysis of SMP according to CO content.

This trend was also confirmed in thermomechanical behavior. Figure 4-3(a) showed the effect of increasing the amount of CO on thermomechanical properties. The storage modulus decreased as the amount of CO increased, and the glass transition temperature (T_g) decreased by 27°C from 88°C to 61°C. As the amount of CO having

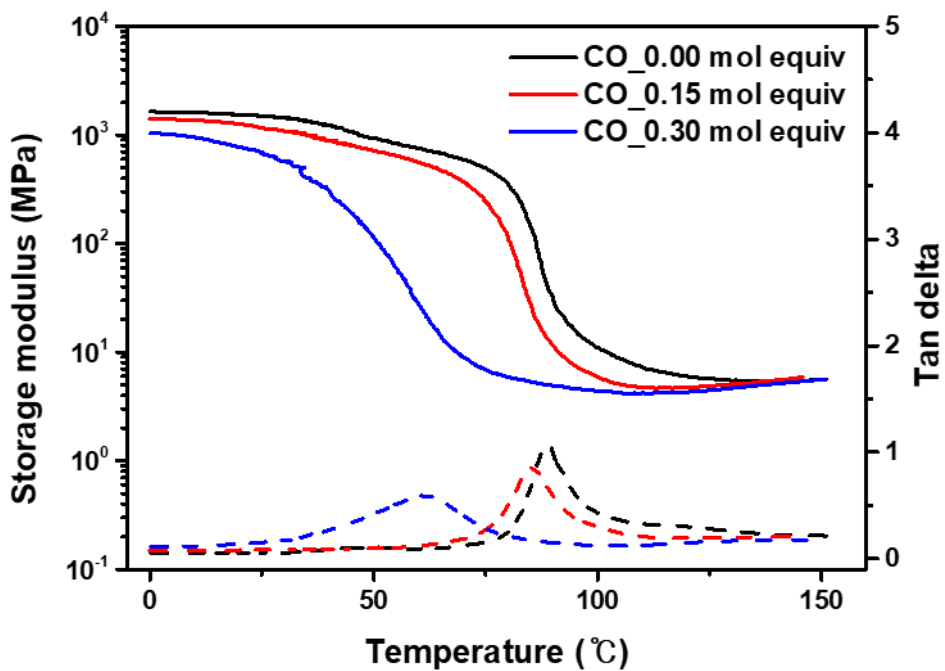
a linear chain structure increased, the flexibility of the polymer chain increased, resulting in a decrease in T_g [119, 120].

In the case of shape memory performance, it was measured by the following process (Figure 4-3(b)). The first was the deformation step. The sample was deformed at a temperature above T_g ($\epsilon_i \rightarrow \epsilon_d$). The second was the fixation step. While maintaining the deformation, the temperature of the sample cooled down below T_g , and the shape was fixed. At this time, by removing the force used for deformation, the sample actually maintained the deformed shape (i.e. temporary shape, $\epsilon_d \rightarrow \epsilon_f$). In this step, the fixity ratio (R_f) could be calculated. The next was the recovery step. While maintaining the force removed, the temperature was raised to a temperature above T_g . At this time, the temporary shape began to recover to the original shape, and the recovery ratio (R_r) could be calculated through the final shape ($\epsilon_f \rightarrow \epsilon_r$). The R_f and R_r was calculated by following equations.

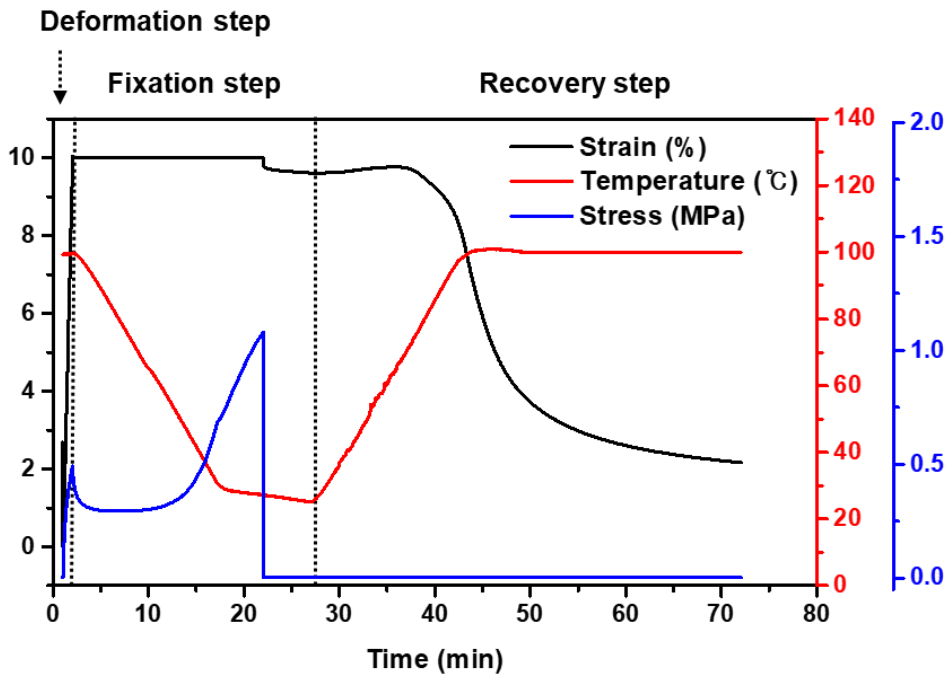
$$R_f(\%) = \frac{\epsilon_f}{\epsilon_d} \times 100 \quad R_r(\%) = \frac{\epsilon_d - \epsilon_r}{\epsilon_d} \times 100$$

Shape memory performance and thermomechanical properties were summarized in Table 4-1. R_f was not significantly affected by the CO content, but R_r was greatly affected. Shape memory behavior is affected by hard segments including physical entanglement and crosslinking, and switching segments including flexible linear chains. The hard segment serves as an anchor, and when the shape is fixed after being deformed, it maintains the deformation state. The switching segment has an effect

on making the shape memory polymer to be more easily deformed and plays a role in recovering the original shape in the recovery process [121]. The increase in CO caused an increase in the switching segment and had a great influence on the recovery process, so the shape recovery ability increased as the CO increased. In addition, it can be confirmed that less stress was required to deform due to the structure of CO.



(a)



(b)

Figure 4-3 (a) Thermomechanical behavior of SMP according to CO content (straight line - storage modulus, dash line - tan delta) and (b) shape memory behavior (CO content: 0.15 mol equivalent to DCPD).

Table 4-1 Thermomechanical and shape memory properties of SMP.

CO mol equiv	Storage modulus of glassy state (GPa)	Glass transition temperature (°C)	Fixity ratio (%)	Recovery ratio (%)	Maximum stress (MPa)
CO 0	1641.81	88.41	95.92	63.54	1.54
CO 0.15	1407.44	85.20	96.13	78.36	1.08
CO 0.3	1017.59	61.72	94.14	89.30	0.50

In consideration of thermomechanical properties and shape memory performance, SMP having a molar equivalent of CO of 0.15 was selected as the 3D printing material. This was because the SMP of this composition did not have much lower mechanical properties than the case without CO and showed satisfactory fixity and recovery ratio.

4.2.2. Rheological properties and frontal velocity

The rheological properties were measured to observe the printability of the ink. Figure 4-4(a) shows the storage modulus and loss modulus as a function of incubation time. The appearance of the extruded ink (Figure 4-4(b)~(g)) according to the incubation time was marked in Figure 4-4(a). In (b) region, the storage modulus was lower than the loss modulus and the viscosity was low, so the ink extruded in the form of droplet. In (c) region, where the vicinity of the intersection of the storage modulus and the loss modulus (i.e. gel point), gelation began and the connected stream line was extruded. In (d) and (e) region, the viscosity became higher so that it was extruded thicker than that of (c) region. The height of the ink piled up on the build plate was increased. However, over time, the accumulated ink fused and sank. In these region, 3D printing was possible if frontal polymerization occurred before the extruded structure was depleted, but free-standing structure could not be printed. In (f) region, the storage modulus increased to a $10^4\sim 10^5$ Pa,

and it was almost solidified. The extruded ink was deposited on the build plate while maintaining its shape, and the newly extruded filaments were fused with the surface of the extruded filament before. In (g) region, the ink was extruded while maintaining its shape, but the extruded ink was not fused together. If the further incubation proceeded, the pressure of the printing head was not sufficient to extrude the ink. By observing the appearance of the extruded ink, it was determined that printing from 165 min to 200 min corresponding to (f) and (g) was possible.

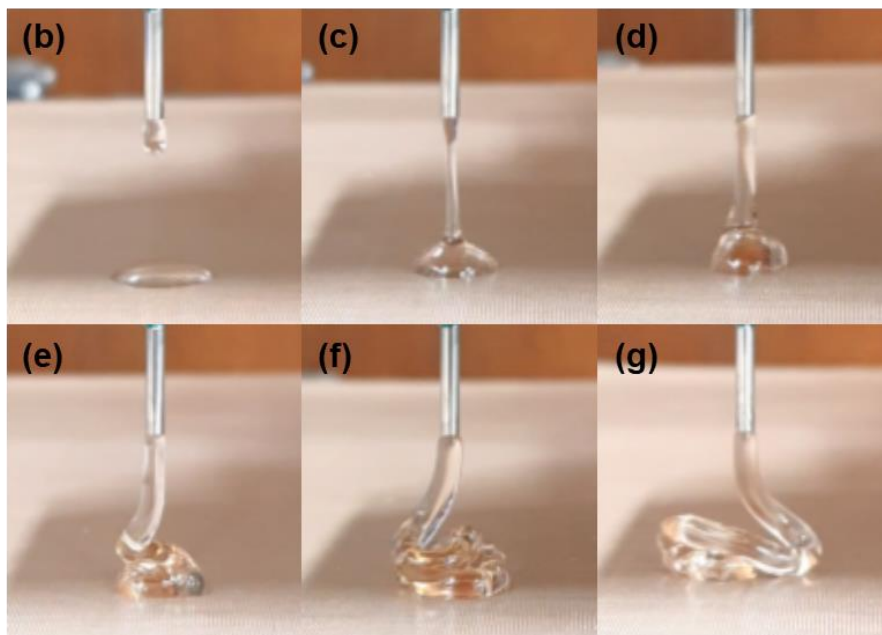
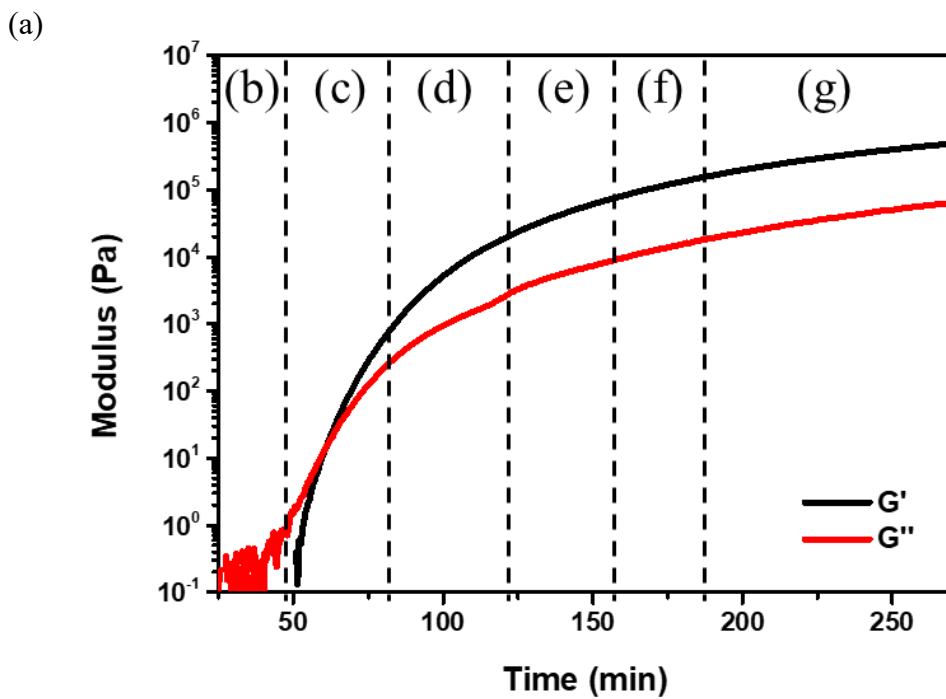


Figure 4-4 (a) Rheological properties of SMP and (b-g) extruded appearance at each state.

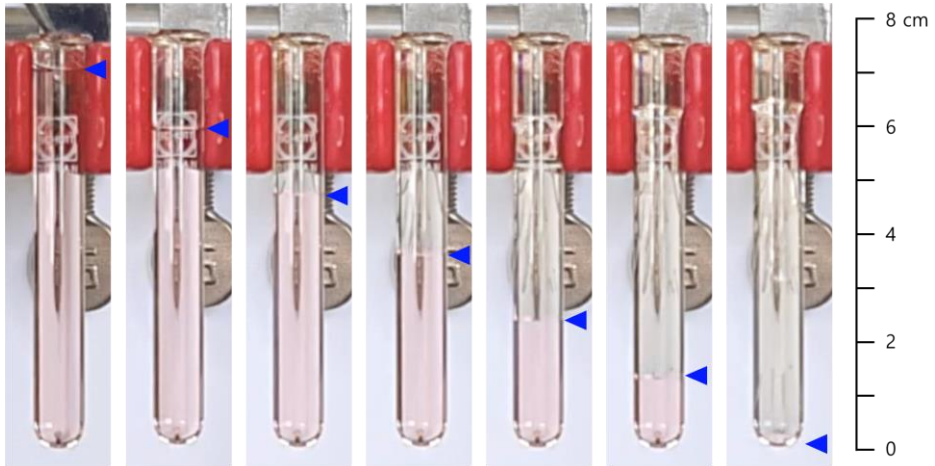
When printing, the distance between the end of the nozzle and the frontal polymerization line was maintained as 10 mm. Therefore, in order to print a free-standing structure, a 10 mm long filament floating in the horizontal direction without any support material must maintain its shape well. Smay et al. applied the Euler-Bernoulli beam theory to calculate the effective homogeneous shear modulus (G'_{eff}) required when a gel ink is printed with cylindrical spanning filaments [122]. G'_{eff} is the shear modulus for the deflection at the center point of the span to be less than 5% of the diameter of the filament. It is calculated by the following equation.

$$G'_{\text{eff}} \geq \frac{1.4\rho gL^4}{D^3}$$

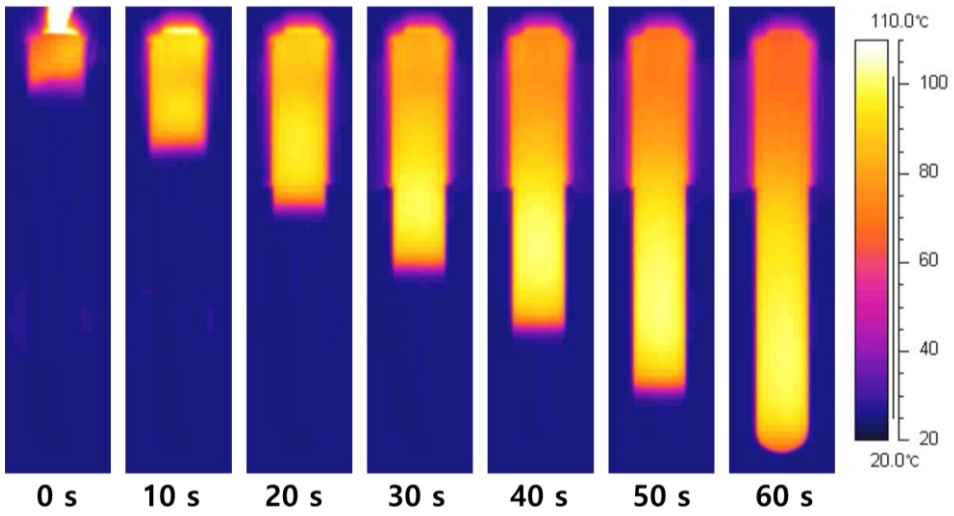
ρ is the density of the gel, g is gravitational acceleration, L is the span distance, and D is the diameter of the filament. In this study, the span distance, the distance between the nozzle and the frontal polymerization line, was 10 mm, the diameter of the filament is 2.5 mm, and the density of the gel was 0.390 g/cm³. According the equation, G'_{eff} should be at least 9226 Pa. The incubation time that satisfies G'_{eff} was 183 min or more, and the printing was possible up to 225 min when using the cooling chamber to delay the rate of gelation.

To determine the printing speed, the frontal velocity was measured and the process was shown in Figure 4-5. Figure 4-5(a) is the frontal polymerization process of the ink incubated for 30 min, and the frontal polymerization line was indicated by blue arrows. When heat was locally applied, polymerization occurred at the local region

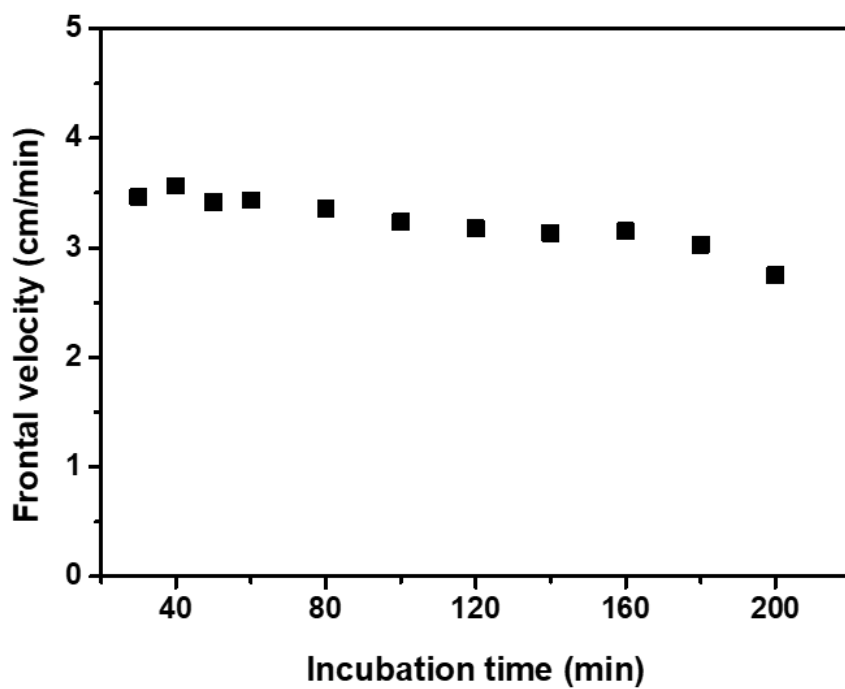
and the heat was generated by polymerization. The heat was transferred to the adjacent monomers and monomers were polymerized. The heat generated by polymerization stimulated the adjacent monomers again. Finally, the polymerization proceeded along the column. Figure 4-5(b) showed that the temperature of the ink which was changed as heat was transferred. As the frontal polymerization line advanced, the temperature of the ink raised to 90°C, and the heat of polymerization was propagated. Accordingly, the frontal velocity according to the incubation time is shown in Figure 4-5(c). The frontal velocity tended to decrease as the incubation time went by, and showed about 3 cm/min in the region when the 3D printing is possible. Therefore, the printing speed was determined to be 3cm/min according to the frontal velocity.



(a)



(b)

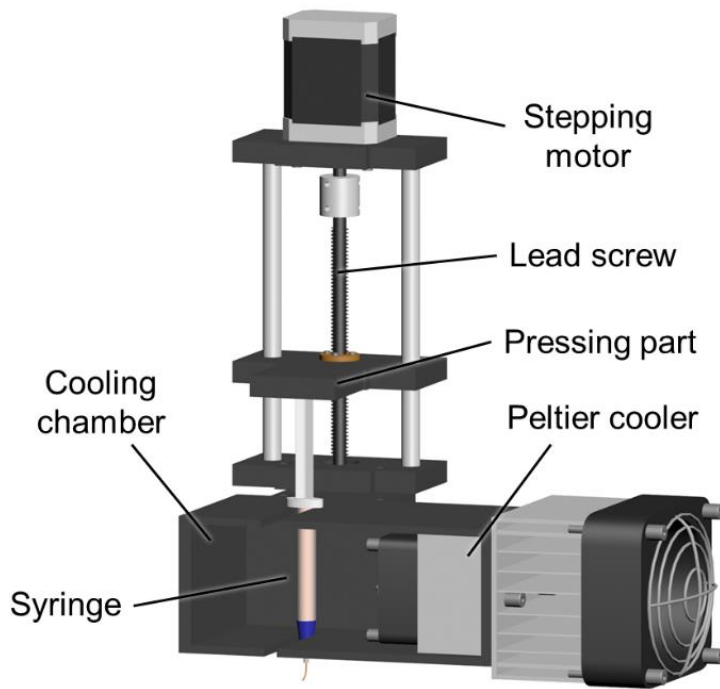


(c)

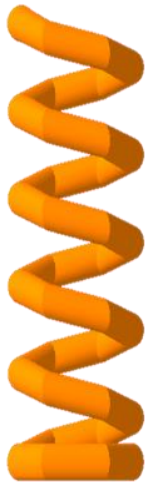
Figure 4-5 (a) Frontal polymerization of frontal SMP ink, (b) IR camera image for frontal velocity measurement (c) frontal velocity according to incubation time.

4.2.3. 3D printing and the shape memory properties of SMP

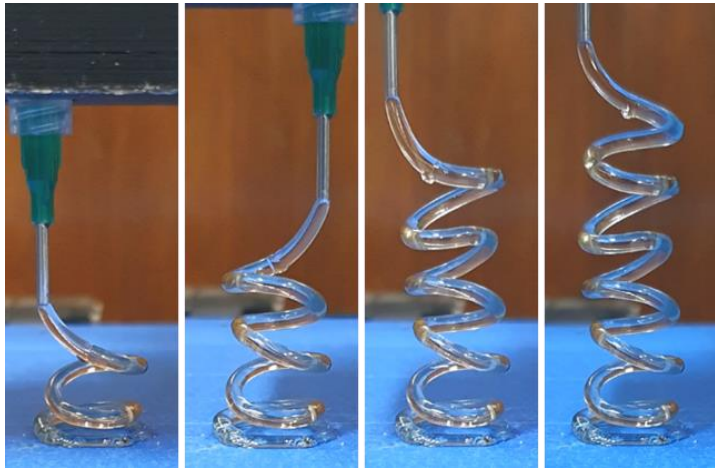
The 3D printing conditions were determined based on the rheological properties of frontal SMP. The 3D printing system consisted of a printing head (Figure 4-6(a)) and an X-Y-Z plot system that could move the printing head in three dimensions. The syringe was placed in a cooling chamber, and the cooling chamber was maintained at -5°C using a Peltier cooler when the printable time reached (incubation time = 183 minutes) through the incubation process. The speed of the stepping motor was adjusted so that the ink could be extruded at a speed of 0.147 mL/min from the nozzle with a diameter of 1.77mm, and the ink was extruded by pushing the piston of the syringe by the pressing part. When printing, the frontal polymerization was initiated by heating at a distance of 10 mm from the nozzle tip.



(a)



(b)



(c)

Figure 4-6 (a) Schematic diagram of printing head, (b) 3D design of free-standing structure and (c) printed product using 3D printing.

To demonstrate that the free-standing structure can be 3D printed, a regular hexagonal spiral structure with a side length of 10 mm and a lead length of 10 mm, such as Figure 4-6(b), was designed. The printed product was shown in Figure 4-6(c). Frontal SMP was able to be successfully printed into the free-standing structure without any supporting material because the frontal polymerization occurred along the printing path and fixed the shape. However, since the distance between the nozzle and the frontal line was maintained at 10mm, there was a difference between the printing path and the shape of the printing product. The product was printed that resembled a circular spiral with softer edges than a regular hexagonal spiral.

The shape memory behavior of the spiral product was observed. Figure 4-7(a) showed a series of shape memory processes in which the product was heated above the transition temperature, stretched in the longitudinal direction, cooled to fix it in a temporary shape, and then heated above the transition temperature to recover its original shape.

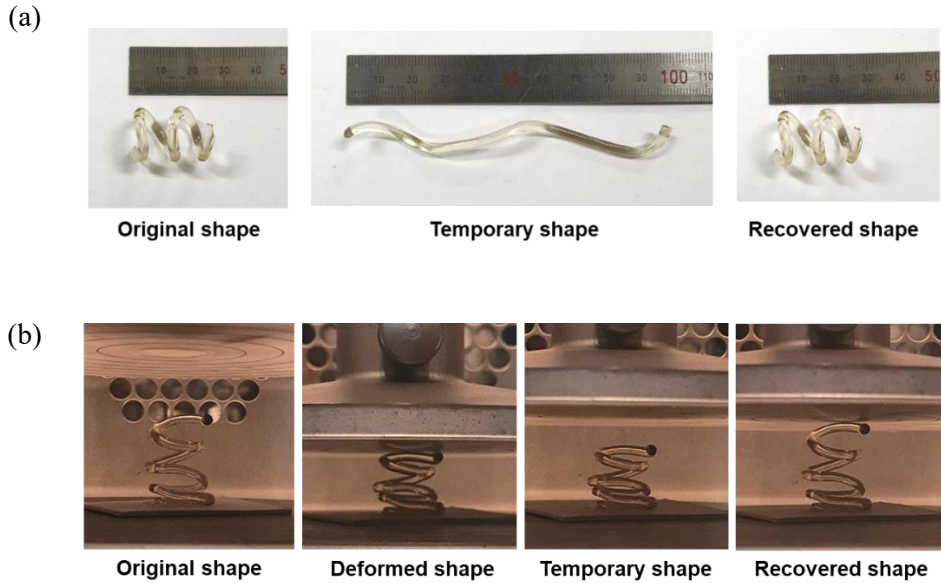


Figure 4-7 Shape memory behavior of 3D printed frontal SMP under (a) tensile deformation and (b) compressive deformation.

Figure 4-7(b) showed the shape memory behavior under compression. The product was compressed by 30% in the longitudinal direction. The shape memory properties were calculated by measuring the length at each step. When calculated through product deformation, the fixity ratio was 94.5(1.6)% and the recovery ratio was 88.8(2.7)% . All of the printed spiral products showed excellent shape memory behavior.

4.3. Summary

A thermosetting SMP capable of 3D printing the free-standing structures have been synthesized. The material has DCPD and CO as monomers, and it can undergo frontal polymerization using GC2 as a catalyst. It was confirmed that it has shape memory capability by analyzing the thermomechanical properties of the material. In addition, the printing conditions were determined in consideration of the rheological properties and the frontal velocity of SMP. The SMP ink for 3D printing went through an incubation process until it had a rheological property (G'_{eff}) suitable for 3D printing of free-standing structures. In conclusion, the 3D printing system for free-standing structures was successfully developed. The 3D SMP product printed by the 3D printing system showed excellent shape memory performance. The system is expected to broaden the application of 4D printing because it can print geometrically more complex 3D structures using SMPs.

Chapter 5. Conclusion

The purpose of this study is to develop a new 3D printing system for SMPC, and to establish a method to characterize the 3D shape memory behavior of the printed SMPC.

First, a method to characterize 3D shape memory behavior was proposed. In this study, we manufactured a miniature model of a deployable antenna in space, one of the popular applications of SMP. The deployable antenna is launched in a folded state from the ground, and acts as an antenna by deploying according to the environmental change in space. It is important to analyze how well the SMP antenna is fixed in the folded state and how well the original shape is restored. However, the existing characterization methods could not characterize the three-dimensional shape memory behavior like the deployable antennas. Therefore, we introduced shape descriptors to analyze the deploying behavior. In particular, the 3d compactness represented the deploying behavior of the antenna properly, and the 3D shape memory properties could be analyzed effectively.

Secondly, in order to print SMPC with enhanced mechanical properties, 3D printing process of CCFRTP was developed. To overcome the existing heavy and uneconomical process, an *in situ* pin-assisted melt impregnation process was introduced. The thermal properties and the printability was investigated to optimizing the printing process. The degree of impregnation was improved

significantly compared to the other printing methods, which enhanced the mechanical properties of 3D printed composites. Finally, SMPC antenna was successfully fabricated via new 3D printing system.

Thirdly, a 3D printing process has been developed for printing thermosetting SMPs with free-standing structures. In 4D printing, it is important to make SMP geometrically complex shapes. Therefore, printing SMPs with free-standing structures without supporting materials has significant advantages. In this study, we synthesized SMP capable of frontal polymerization and succeeded in printing a free-standing structure of SMP by controlling the rheological properties of this material. And it was confirmed that the printed SMP has good shape memory performance.

Using the 3D characterization method and the new 3D printing systems presented in this study, the stronger and more complex practical shapes can be 3D printed. In addition, the method of analyzing thermomechanical and rheological properties and the method of investigating printability are likely to help in the development of the other 3D printing processes.

Reference

1. Lendlein, A., *Shape-memory polymers*. Vol. 226. 2010: Springer.
2. Firouzeh, A., M. Salerno, and J. Paik, *Stiffness control with shape memory polymer in underactuated robotic origamis*. IEEE Transactions on Robotics, 2017. **33**(4): p. 765-777.
3. Hines, L., V. Arabagi, and M. Sitti, *Shape Memory Polymer-Based Flexure Stiffness Control in a Miniature Flapping-Wing Robot*. IEEE Transactions on Robotics, 2012. **28**(4): p. 987-990.
4. Jin, B., et al., *Programming a crystalline shape memory polymer network with thermo-and photo-reversible bonds toward a single-component soft robot*. Science advances, 2018. **4**(1): p. eaao3865.
5. Monkman, G.J., *Advances in shape memory polymer actuation*. Mechatronics, 2000. **10**(4): p. 489-498.
6. An, Y., et al., *Quantitative evaluation of the three-dimensional deployment behavior of a shape memory polymer antenna*. Smart Materials and Structures, 2018. **27**(10): p. 105007.
7. Dao, T.D., et al., *Design, fabrication, and bending test of shape memory polymer composite hinges for space deployable structures*. Journal of Intelligent Material Systems and Structures, 2017. **29**(8): p. 1560-1574.
8. Fabrizio, Q., S. Loredana, and S.E. Anna, *Shape memory epoxy foams for space applications*. Materials Letters, 2012. **69**: p. 20-23.
9. Gall, K., et al., *Carbon Fiber Reinforced Shape Memory Polymer Composites*. Journal of Intelligent Material Systems and Structures, 2000. **11**(11): p. 877-886.
10. Jang, J.H., et al., *Long-term properties of carbon fiber-reinforced shape memory epoxy/polymer composites exposed to vacuum and ultraviolet radiation*. Smart Materials and Structures, 2019. **28**(11): p. 115013.
11. Liu, T., et al., *Integrative hinge based on shape memory polymer composites: Material, design, properties and application*. Composite Structures, 2018. **206**: p. 164-176.
12. Liu, Y., et al., *Shape memory polymers and their composites in aerospace applications: a review*. Smart Materials and Structures, 2014. **23**(2): p.

023001.

13. Yoon, J., et al., *Fabrication of a Highly Stretchable, Wrinkle-Free Electrode with Switchable Transparency Using a Free-Standing Silver Nanofiber Network and Shape Memory Polymer Substrate*. *Macromolecular Rapid Communications*, 2020. **41**(13): p. 2000129.
14. Gao, H., et al., *The research status and challenges of shape memory polymer-based flexible electronics*. *Materials Horizons*, 2019. **6**(5): p. 931-944.
15. Wang, X., et al., *Freestanding 3D Mesostuctures, Functional Devices, and Shape-Programmable Systems Based on Mechanically Induced Assembly with Shape Memory Polymers*. *Advanced Materials*, 2019. **31**(2): p. 1805615.
16. Yu, Z., et al., *Highly flexible silver nanowire electrodes for shape-memory polymer light-emitting diodes*. *Advanced Materials*, 2011. **23**(5): p. 664-668.
17. Zarek, M., et al., *3D printing of shape memory polymers for flexible electronic devices*. *Advanced Materials*, 2016. **28**(22): p. 4449-4454.
18. Govindarajan, T. and R. Shandas, *A survey of surface modification techniques for next-generation shape memory polymer stent devices*. *Polymers*, 2014. **6**(9): p. 2309-2331.
19. Yakacki, C.M., et al., *Unconstrained recovery characterization of shape-memory polymer networks for cardiovascular applications*. *Biomaterials*, 2007. **28**(14): p. 2255-2263.
20. Jing, X., et al., *Shape memory thermoplastic polyurethane (TPU)/poly (ϵ -caprolactone)(PCL) blends as self-knotting sutures*. *journal of the mechanical behavior of biomedical materials*, 2016. **64**: p. 94-103.
21. Lendlein, A. and R. Langer, *Biodegradable, elastic shape-memory polymers for potential biomedical applications*. *Science*, 2002. **296**(5573): p. 1673-1676.
22. Wache, H., et al., *Development of a polymer stent with shape memory effect as a drug delivery system*. *Journal of Materials Science: Materials in Medicine*, 2003. **14**(2): p. 109-112.

23. Keller, P., et al. *Development of elastic memory composite stiffeners for a flexible precision reflector*. in *47th AIAA/ASME/ASCE/AHS/ASC Structures, Structural Dynamics, and Materials Conference 14th AIAA/ASME/AHS Adaptive Structures Conference 7th*. 2006.
24. Lin, J., C. Knoll, and C. Willey. *Shape memory rigidizable inflatable (RI) structures for large space systems applications*. in *47th AIAA/ASME/ASCE/AHS/ASC Structures, Structural Dynamics, and Materials Conference 14th AIAA/ASME/AHS Adaptive Structures Conference 7th*. 2006.
25. Wang, W., H. Rodrigue, and S.-H. Ahn, *Deployable soft composite structures*. Scientific reports, 2016. **6**(1): p. 1-10.
26. Ge, Q., et al., *Active origami by 4D printing*. Smart Materials and Structures, 2014. **23**(9): p. 094007.
27. Gladman, A.S., et al., *Biomimetic 4D printing*. Nature materials, 2016. **15**(4): p. 413-418.
28. Mao, Y., et al., *3D printed reversible shape changing components with stimuli responsive materials*. Scientific reports, 2016. **6**(1): p. 1-13.
29. Mao, Y., et al., *Sequential self-folding structures by 3D printed digital shape memory polymers*. Scientific reports, 2015. **5**: p. 13616.
30. Wu, J., et al., *Multi-shape active composites by 3D printing of digital shape memory polymers*. Scientific reports, 2016. **6**: p. 24224.
31. Lu, H. and S. Du, *A phenomenological thermodynamic model for the chemo-responsive shape memory effect in polymers based on Flory–Huggins solution theory*. Polymer Chemistry, 2014. **5**(4): p. 1155-1162.
32. Sun, L., et al., *Stimulus-responsive shape memory materials: a review*. Materials & Design, 2012. **33**: p. 577-640.
33. Beavers, F., et al. *Design and testing of an elastic memory composite deployment hinge for spacecraft*. in *43rd AIAA/ASME/ASCE/AHS/ASC Structures, Structural Dynamics, and Materials Conference*. 2002.
34. Francis, W., et al. *Development and testing of a hinge/actuator using elastic memory composites*. in *44th AIAA/ASME/ASCE/AHS/ASC Structures, Structural Dynamics, and Materials Conference*. 2003.

35. Lan, X., et al., *Fiber reinforced shape-memory polymer composite and its application in a deployable hinge*. Smart Materials and Structures, 2009. **18**(2): p. 024002.
36. Tupper, M., et al. *Developments in elastic memory composite materials for spacecraft deployable structures*. in *2001 IEEE Aerospace Conference Proceedings (Cat. No. 01TH8542)*. 2001. IEEE.
37. Campbell, D., et al. *Elastic memory composite material: an enabling technology for future furlable space structures*. in *46th AIAA/ASME/ASCE/AHS/ASC Structures, Structural Dynamics and Materials Conference*. 2005.
38. Keller, P., et al. *Development of a deployable boom for microsattellites using elastic memory composite material*. in *45th AIAA/ASME/ASCE/AHS/ASC Structures, Structural Dynamics & Materials Conference*. 2004.
39. Lake, M., et al. *Application of elastic memory composite materials to deployable space structures*. in *AIAA Space 2001 Conference and Exposition*. 2001.
40. Arzberger, S.C., et al. *Elastic memory composites (EMC) for deployable industrial and commercial applications*. in *Smart structures and materials 2005: industrial and commercial applications of smart structures technologies*. 2005. International Society for Optics and Photonics.
41. Barrett, R., et al. *Design of a solar array to meet the standard bus specification for operation responsive space*. in *48th AIAA/ASME/ASCE/AHS/ASC Structures, Structural Dynamics, and Materials Conference*. 2007.
42. Yin, W., J. Liu, and J. Leng, *Deformation analysis of shape memory polymer for morphing wing skin under airflow*. Frontiers of Mechanical Engineering in China, 2009. **4**(4): p. 447.
43. Bye, D. and P. McClure. *Design of a morphing vehicle*. in *48th AIAA/ASME/ASCE/AHS/ASC structures, structural dynamics, and materials conference*. 2007.
44. Hinkle, J., J. Lin, and D. Kling. *Design and materials study on secondary*

- structures in deployable planetary and space habitats.* in *52nd AIAA/ASME/ASCE/AHS/ASC Structures, Structural Dynamics and Materials Conference 19th AIAA/ASME/AHS Adaptive Structures Conference 13t.* 2014.
45. Schonberg, W., F. Schäfer, and R. Putzar, *Some comments on the protection of lunar habitats against damage from meteoroid impacts.* Journal of Aerospace Engineering, 2010. **23**(1): p. 90-97.
 46. Wagermaier, W., et al., *Characterization methods for shape-memory polymers,* in *Shape-memory polymers.* 2009, Springer. p. 97-145.
 47. Lu, H., et al., *Heating/ethanol-response of poly methyl methacrylate (PMMA) with gradient pre-deformation and potential temperature sensor and anti-counterfeit applications.* Smart materials and structures, 2014. **23**(6): p. 067002.
 48. Lendlein, A. and S. Kelch, *Shape-memory polymers.* Angewandte Chemie International Edition, 2002. **41**(12): p. 2034-2057.
 49. Momeni, F., et al., *A review of 4D printing.* Materials & Design, 2017. **122**: p. 42-79.
 50. Bakarich, S.E., et al., *4D printing with mechanically robust, thermally actuating hydrogels.* Macromolecular rapid communications, 2015. **36**(12): p. 1211-1217.
 51. Guo, J., et al., *4D printing of robust hydrogels consisted of agarose nanofibers and polyacrylamide.* ACS Macro Letters, 2018. **7**(4): p. 442-446.
 52. Hu, Y., et al., *Botanical-inspired 4D printing of hydrogel at the microscale.* Advanced Functional Materials, 2020. **30**(4): p. 1907377.
 53. Naficy, S., et al., *4D printing of reversible shape morphing hydrogel structures.* Macromolecular Materials and Engineering, 2017. **302**(1): p. 1600212.
 54. Choong, Y.Y.C., et al., *4D printing of high performance shape memory polymer using stereolithography.* Materials & Design, 2017. **126**: p. 219-225.
 55. Ding, Z., et al., *Direct 4D printing via active composite materials.* Science advances, 2017. **3**(4): p. e1602890.

56. Ge, Q., et al., *Multimaterial 4D printing with tailorable shape memory polymers*. Scientific reports, 2016. **6**: p. 31110.
57. Wei, H., et al., *Direct-write fabrication of 4D active shape-changing structures based on a shape memory polymer and its nanocomposite*. ACS applied materials & interfaces, 2017. **9**(1): p. 876-883.
58. Zhang, Y., et al., *4D printing of a digital shape memory polymer with tunable high performance*. ACS applied materials & interfaces, 2019. **11**(35): p. 32408-32413.
59. Park, S.J. and M.K. Seo, *Carbon fiber-reinforced polymer composites: preparation, properties, and applications*. Polymer composites, 2012: p. 135-183.
60. Yang, H., et al., *Continuous and rapid production of three-dimensional woven fabric preforms using a new weaving technique*. Functional Composites and Structures, 2020. **2**(1): p. 015005.
61. Sung, M., et al., *Increased breaking strain of carbon fiber-reinforced plastic and steel hybrid laminate composites*. Composite Structures, 2020. **235**: p. 111768.
62. Yao, S.-S., et al., *Recent advances in carbon-fiber-reinforced thermoplastic composites: A review*. Composites Part B: Engineering, 2018. **142**: p. 241-250.
63. Ning, F., et al., *Additive manufacturing of carbon fiber reinforced thermoplastic composites using fused deposition modeling*. Composites Part B: Engineering, 2015. **80**: p. 369-378.
64. Jin, F.-L. and S.-J. Park, *Preparation and characterization of carbon fiber-reinforced thermosetting composites: a review*. Carbon Letters (Carbon Lett.), 2015. **16**(2): p. 67-77.
65. Chang, B., et al., *Ultrafast printing of continuous fiber-reinforced thermoplastic composites with ultrahigh mechanical performance by ultrasonic-assisted laminated object manufacturing*. Polymer Composites. **n/a**(n/a).
66. Mori, K.-i., T. Maeno, and Y. Nakagawa, *Dieless forming of carbon fibre reinforced plastic parts using 3D printer*. Procedia engineering, 2014. **81**:

- p. 1595-1600.
67. Bettini, P., et al., *Fused Deposition Technique for Continuous Fiber Reinforced Thermoplastic*. Journal of Materials Engineering and Performance, 2017. **26**(2): p. 843-848.
 68. Blok, L.G., et al., *An investigation into 3D printing of fibre reinforced thermoplastic composites*. Additive Manufacturing, 2018. **22**: p. 176-186.
 69. Botelho, E., M. Rezende, and B. Lauke, *Mechanical behavior of carbon fiber reinforced polyamide composites*. Composites Science and Technology, 2003. **63**(13): p. 1843-1855.
 70. Mark, G.T. and A.S. Gozdz, *Three dimensional printer with composite filament fabrication*. 2015, Google Patents.
 71. Matsuzaki, R., et al., *Three-dimensional printing of continuous-fiber composites by in-nozzle impregnation*. Scientific Reports, 2016. **6**(1): p. 23058.
 72. Qureshi, Z., et al., *In situ consolidation of thermoplastic prepreg tape using automated tape placement technology: Potential and possibilities*. Composites Part B: Engineering, 2014. **66**: p. 255-267.
 73. Yassin, K. and M. Hojjati, *Processing of thermoplastic matrix composites through automated fiber placement and tape laying methods:A review*. Journal of Thermoplastic Composite Materials, 2018. **31**(12): p. 1676-1725.
 74. Tian, X., et al., *Interface and performance of 3D printed continuous carbon fiber reinforced PLA composites*. Composites Part A: Applied Science and Manufacturing, 2016. **88**: p. 198-205.
 75. Liu, T., et al., *Interfacial performance and fracture patterns of 3D printed continuous carbon fiber with sizing reinforced PA6 composites*. Composites Part A: Applied Science and Manufacturing, 2018. **114**: p. 368-376.
 76. Li, N., Y. Li, and S. Liu, *Rapid prototyping of continuous carbon fiber reinforced polylactic acid composites by 3D printing*. Journal of Materials Processing Technology, 2016. **238**: p. 218-225.
 77. Peltonen, P., et al., *The influence of melt impregnation parameters on the degree of impregnation of a polypropylene/glass fibre prepreg*. Journal

- of Thermoplastic Composite Materials, 1992. **5**(4): p. 318-343.
78. Liu, T., et al., *High-pressure interfacial impregnation by micro-screw in-situ extrusion for 3D printed continuous carbon fiber reinforced nylon composites*. Composites Part A: Applied Science and Manufacturing, 2020. **130**: p. 105770.
79. Jiang, Z., et al., *Extrusion 3D Printing of Polymeric Materials with Advanced Properties*. Advanced Science, 2020. **7**(17): p. 2001379.
80. Shi, Q., et al., *Recyclable 3D printing of vitrimer epoxy*. Materials Horizons, 2017. **4**(4): p. 598-607.
81. Standard, A., *Standard terminology for additive manufacturing technologies*. ASTM International F2792-12a, 2012.
82. Compton, B.G. and J.A. Lewis, *3D-printing of lightweight cellular composites*. Advanced materials, 2014. **26**(34): p. 5930-5935.
83. Chandrasekaran, S., et al., *3D printing of high performance cyanate ester thermoset polymers*. Journal of Materials Chemistry A, 2018. **6**(3): p. 853-858.
84. Lewicki, J.P., et al., *3D-printing of meso-structurally ordered carbon fiber/polymer composites with unprecedented orthotropic physical properties*. Scientific reports, 2017. **7**(1): p. 1-14.
85. Gall, K., et al., *Thermomechanics of the shape memory effect in polymers for biomedical applications*. Journal of Biomedical Materials Research Part A: An Official Journal of The Society for Biomaterials, The Japanese Society for Biomaterials, and The Australian Society for Biomaterials and the Korean Society for Biomaterials, 2005. **73**(3): p. 339-348.
86. Liu, Y., et al., *Thermomechanical recovery couplings of shape memory polymers in flexure*. Smart Materials and Structures, 2003. **12**(6): p. 947.
87. Seffen, K., Z. You, and S. Pellegrino, *Folding and deployment of curved tape springs*. International Journal of Mechanical Sciences, 2000. **42**(10): p. 2055-2073.
88. Lin, J. and L. Chen, *Study on shape-memory behavior of polyether-based polyurethanes. I. Influence of the hard-segment content*. Journal of applied polymer science, 1998. **69**(8): p. 1563-1574.

89. Li, G. and N. Uppu, *Shape memory polymer based self-healing syntactic foam: 3-D confined thermomechanical characterization*. Composites Science and Technology, 2010. **70**(9): p. 1419-1427.
90. Hassan, M.S., *Crease recovery properties of cotton fabrics modified by urea resins under the effect of gamma irradiation*. Radiation Physics and Chemistry, 2009. **78**(5): p. 333-337.
91. Liu, X., et al., *Elasticity and shape memory effect of shape memory fabrics*. Textile Research Journal, 2008. **78**(12): p. 1048-1056.
92. Flusser, J., B. Zitova, and T. Suk, *Moments and moment invariants in pattern recognition*. 2009: John Wiley & Sons.
93. Barrett, R., et al., *Deployable reflectors for small satellites*. 2007.
94. Rosin, P.L., *Measuring shape: ellipticity, rectangularity, and triangularity*. Machine Vision and Applications, 2003. **14**(3): p. 172-184.
95. Stutzman, W.L. and G.A. Thiele, *Antenna theory and design*. 2012: John Wiley & Sons.
96. Park, H., et al., *Three-dimensional constitutive model for shape memory polymers using multiplicative decomposition of the deformation gradient and shape memory strains*. Mechanics of Materials, 2016. **93**: p. 43-62.
97. Sadjadi, F.A. and E.L. Hall, *Three-dimensional moment invariants*. IEEE Transactions on Pattern Analysis and Machine Intelligence, 1980(2): p. 127-136.
98. Martinez-Ortiz, C.A., *2D and 3D shape descriptors*. 2010.
99. Sonka, M., V. Hlavac, and R. Boyle, *Image Processing, Analysis, and Machine Vision (Boston, MA: Cengage Learning)*. 2014.
100. Žunić, J., K. Hirota, and C. Martinez-Ortiz. *Compactness measure for 3d shapes*. in *2012 International Conference on Informatics, Electronics & Vision (ICIEV)*. 2012. IEEE.
101. Martinez-Ortiz, C. and J. Žunić. *Measuring cubeness of 3d shapes*. in *Iberoamerican Congress on Pattern Recognition*. 2009. Springer.
102. Glemet, M. and G. Cognet, *Process for the manufacture of sections of thermoplastic resin reinforced with continuous fibers*. 1989, Google Patents.

103. Dyksterhouse, J.A., *Method of prepregging with resin and novel prepregs produced by such method*. 2003, Google Patents.
104. Hilakos, W., *Apparatus and method for impregnating continuous lengths of multifilament and multi-fiber structures*. 1989, Google Patents.
105. Yoon, B.S., S.H. Lee, and M.H. Suh, *Continuous glass-fiber reinforced nylon 6 by using a new impregnation die*. *Polymer composites*, 1997. **18**(5): p. 656-662.
106. Henninger, F. and K. Friedrich, *Thermoplastic filament winding with online-impregnation. Part A: process technology and operating efficiency*. *Composites Part A: Applied Science and Manufacturing*, 2002. **33**(11): p. 1479-1486.
107. Unger, M., *Method and apparatus for manufacturing fibre-reinforcing material*. 1992, Google Patents.
108. Vlug, M.A., *Process of melt impregnation*. 1998, Google Patents.
109. Thorfinnson, B. and T. Biermann, *Degree of Impregnation of Prepregs-- Effects on Porosity*. *Advanced Materials Technology'87*, 1987: p. 1500-1509.
110. Bijsterbosch, H. and R.J. Gaymans, *Impregnation of glass rovings with a polyamide melt. Part 1: Impregnation bath*. *Composites Manufacturing*, 1993. **4**(2): p. 85-92.
111. Robertson, I.D., et al., *Rapid energy-efficient manufacturing of polymers and composites via frontal polymerization*. *Nature*, 2018. **557**(7704): p. 223-227.
112. Robertson, I.D., et al., *Rapid stiffening of a microfluidic endoskeleton via frontal polymerization*. *ACS Applied Materials & Interfaces*, 2014. **6**(21): p. 18469-18474.
113. Luo, X. and P.T. Mather, *Preparation and characterization of shape memory elastomeric composites*. *Macromolecules*, 2009. **42**(19): p. 7251-7253.
114. Kuang, W. and P.T. Mather, *Tuning of reversible actuation via ROMP-based copolymerization semicrystalline polymers*. *Polymer*, 2018. **156**: p. 228-239.
115. Martinez, H., et al., *Ring-opening metathesis polymerization of 8-membered cyclic olefins*. *Polymer Chemistry*, 2014. **5**(11): p. 3507-3532.

116. Kovacic, S. and C. Slugovc, *Ring-opening Metathesis Polymerisation derived poly (dicyclopentadiene) based materials*. Materials Chemistry Frontiers, 2020.
117. Liu, H., H. Wei, and J.S. Moore, *Frontal Ring-Opening Metathesis Copolymerization: Deviation of Front Velocity from Mixing Rules*. ACS Macro Letters, 2019. **8**(7): p. 846-851.
118. Zong, R., et al., *Thermal degradation kinetics of polyethylene and silane-crosslinked polyethylene*. Journal of applied polymer science, 2005. **98**(3): p. 1172-1179.
119. Alonso-Villanueva, J., et al., *Ring-Opening Metathesis Polymerization Kinetics of Cyclooctene with Second Generation Grubbs' Catalyst*. Journal of Macromolecular Science, Part A: Pure and Applied Chemistry, 2010. **47**(11): p. 1130-1134.
120. Wang, H., et al., *Effect of Microstructure on Chain Flexibility and Glass Transition Temperature of Polybenzofulvene*. Polymer, 2020: p. 123276.
121. Lendlein, A. and S. Kelch, *Shape-Memory Polymers*. Angewandte Chemie International Edition, 2002. **41**(12): p. 2034-2057.
122. Smay, J.E., J. Cesarano, and J.A. Lewis, *Colloidal Inks for Directed Assembly of 3-D Periodic Structures*. Langmuir, 2002. **18**(14): p. 5429-5437.

Korean abstract

4D 프린팅은 3D 프린팅된 물체가 시간이 지남에 따라 자신의 모양이나 성질을 변화시킬 수 있는 첨단기술이다. 형상기억고분자는 4D 프린팅의 대표적인 소재이다. 이 연구에서는 기존의 형상기억고분자 프린팅 기술들의 단점을 개선하는 새로운 3D 프린팅 방법이 개발되었다.

3D 프린팅된 형상기억고분자의 3차원 형상 변화를 분석하기 위해 3차원의 특성화 방법이 제시되었다. 3차원 형상기술자를 활용하여 형상기억고분자의 3차원 전개 거동이 정량적으로 분석되었다. 형상기술자란 주어진 3차원 물체의 형상 정보를 대표할 수 있는 수치로 표현되는 값이다. 3차원 형상 변형 거동을 분석하기 위해 에폭시 기반의 형상기억고분자를 이용하여 우주 전개용 안테나를 제조하였다. 우선, 안테나가 전개하는 동안의 3차원 형상을 스캔하고, 2차원과 3차원 형상기술자를 이용하여 이를 분석하여 어떤 형상기술자가 안테나의 전개거동을 기술하는 데 적합한지 조사하였다. 3차원 형상기술자는 2차원 형상 정보에 더해 높이 정보를 제공하기 때문에 접힘-전개 거동에서 나타나는 형상의 변화를 보다 정확하고 민감하게 반영할 수 있다. 그 중에서도 3차원 Compactness가 안테나의 접힘-전개 거동을 기술하는 데 가장 적합한 것으로 나타났다. 에폭시 기반의 형상기억고분자의 1차원 형상기억성능은 고정률이 98%, 회복률이 79%이지만, Compactness를 이용하여 3차원 전개 거동을 분석했을 때에는 고정률이 100%, 회복률이 99.5%를 나타냈다. 이것은 3차원 분석 기술의 필요성과 적절성을 보여준다.

형상기억고분자의 약한 기계적 강도를 보완하기 위해, 연속섬유강화 열가소성 형상기억고분자의 새로운 3D 프린팅 시스템이 개발되었다. 연속

섬유강화 열가소성 고분자는 가볍고, 강하기 때문에 널리 사용되지만, 일반적으로 무겁고 비싼 장비를 사용하여 제조된다. 최근에는 소형, 소량의 연속섬유강화 복합재료를 제조하기 위해 3D 프린팅 기술이 도입되었다. 이 연구에서는 핀보조 용융 함침 방법을 활용하여, 함침과 프린팅 공정이 동시에 진행될 수 있는 3D 프린팅 시스템을 개발하였다. 이 장비의 프린터빌러티와 함침도를 평가하여 프린팅 조건을 결정하였고, 인장 시험을 위한 시편이 프린팅 되었다. 이 시스템을 활용하여 프린팅한 인장 시편의 기계적 물성과 다른 프린팅 시스템으로 프린팅한 시편들의 기계적 물성이 비교되었다. 이 연구에서 개발된 3D 프린팅 시스템으로 만들어진 시편은 함침도가 우수했고, 결과적으로 우수한 기계적 물성을 보였다. 최종적으로 연속섬유강화 형상기억고분자 복합재료로 만든 안테나가 3D 프린팅되었고, 형상기억자를 이용하여 안테나의 형상기억거동을 분석하였다.

4D 프린팅용 재료 중에서 열경화성 고분자는 강한 기계적 물성, 화학적 안정성, 내용제성 등으로 인해 매우 유망한 재료이다. 정면 중합이 가능한 열경화성 재료를 사용하면, 형상의 복잡성을 높일 수 있는 프리스탠딩 구조를 3D 프린팅할 수 있다. 이 연구에서는 poly(dicyclooctene) 네트워크에 스위칭 세그먼트를 만들 수 있는 cyclooctene을 추가하여 정면 중합이 가능한 열경화성 형상기억고분자를 합성하였다. 열기계적 분석 결과 이 재료는 형상기억거동을 보이는 것으로 확인되었다. 프리스탠딩 구조를 프린팅할 수 있는 effective homogeneous shear modulus를 가질 수 있도록 이 재료의 유연학적 성질이 조절되었다. 이 재료의 유연학적 성질과 정면 중합 속도를 바탕으로 프린팅 조건을 결정하고, 프리스탠딩 구조의 육각 나선 물체가 성공적으로 프린팅되었다. 프린팅된 육각 나선은 훌륭한 형상기억성질을 보였다.

핵심어: 형상기억고분자 복합재료, 형상기술자, 연속 섬유 강화 고분자
복합재료, 4D 프린팅, 정면 중합

학번: 2015-20839